Simulating Wind Channelling over Frobisher Bay and its Interaction with Downslope Winds during the 7–8 November 2006 Wind Event

Daniel Deacu[1,2,*], Ayrton Zadra[2] and John Hanesiak[3]

[1]*Centre for Earth Observation Science, Department of Environment and Geography*
University of Manitoba, Winnipeg, Manitoba
[2]*Meteorological Research Division, Environment Canada, Dorval, Québec*
[3]*Centre for Earth Observation Science, Department of Environment and Geography*
University of Manitoba, Winnipeg, Manitoba

[Original manuscript received 10 June 2009; accepted 9 February 2010]

ABSTRACT *Previous observational studies have identified wind channelling over Frobisher Bay induced by pressure fields associated with cyclones as the main cause for the occurrence of strong and sustained surface winds at Iqaluit. The wind event of 7–8 November 2006, when a surface cyclone moved over the Labrador Sea, is representative of many such occurrences. Our simulations of the event with the Global Environmental Multiscale – Limited Area Model (GEM-LAM 2.5 km) show an almost simultaneous development of wind channelling over Frobisher Bay and of downslope winds over the lee slopes of Hall Peninsula, as well as their interaction. The winds are caused by the passage of the same cyclone, but they advect different air masses. The channelled wind is initiated by a barrier jet generated as a result of the low-level blocking of northeasterly winds by steep orography near the head of the bay. Later, it intensifies, while being driven primarily by large-scale pressure gradients. The cross-bay development of the channelled wind against the downslope wind over the lee slopes of Hall Peninsula explains the shift in surface wind direction and the high surface wind speeds recorded at Iqaluit. Some of the findings are also supported by data from radiosondes launched at Iqaluit. A short sensitivity study shows the beneficial effect of a distributed orographic drag parametrization on the near-surface winds. The impact of using a modified Lenderink-Holtslag mixing length and of increasing the vertical resolution near the surface are also addressed.*

RÉSUMÉ *[Traduit par la rédaction] Des études observationnelles précédentes ont identifié la canalisation du vent dans la baie de Frobisher produite par les champs de pression liés aux dépressions comme la cause principale de vents de surface forts et soutenus à Iqaluit. L'événement de vent survenu les 7 et 8 novembre 2006, lorsqu'une dépression en surface s'est déplacée au-dessus de la mer du Labrador, est représentatif de bon nombre de ces situations. Nos simulations de l'événement avec le GEM-LAM 2,5 km (Modèle global environnemental multi-échelle à aire limitée) montrent l'apparition presque simultanée d'une canalisation du vent dans la baie de Frobisher et de vents descendant les pentes sous le vent de la péninsule Hall ainsi que de leur interaction. Les vents sont causés par le passage de la même dépression mais ils advectent des masses d'air différentes. Le vent canalisé est amorcé par un courant-jet de barrière résultant du blocage à basse altitude des vents du nord-est par les pentes escarpées qui bordent le fond de la baie. Plus tard, il s'intensifie, principalement sous l'effet des gradients de pression à grande échelle. La formation du vent canalisé en travers de la baie au-dessus du vent descendant les pentes sous le vent dans la péninsule Hall explique le changement de direction du vent de surface et les vitesses élevées du vent de surface enregistrés à Iqaluit. Certains résultats sont également confirmés par des données de radiosondes lancées à Iqaluit. Une courte étude de sensibilité montre l'effet favorable d'une paramétrisation distribuée du frottement orographique sur les vents près de la surface. Nous étudions aussi l'effet de l'utilisation d'une longueur de mélange de Lenderink-Holtslag modifiée et d'un accroissement de la résolution verticale près de la surface.*

1 Introduction

Numerous studies have investigated topographically induced flows, such as barrier jets and channelled, gap and downslope winds, some have identified the basic physical mechanisms behind their generation and evolution (e.g., Klemp and Lilly, 1975; Parish, 1982; Durran, 1986; Whiteman and Doran, 1993; Mayr et al., 2007). Whiteman and Doran (1993), for

*Corresponding author's e-mail: daniel.deacu@ec.gc.ca; mailing address: Environment Canada, Meteorological Research Division, 2121 TransCanada Highway, 5th Floor, Dorval, Québec, H9P 1J3.

instance, summarized the mechanisms that produce channelled winds, namely, downward momentum transfer, thermally driven, pressure-driven, and forced channelling. These allowed for the explanation of the highly bidirectional wind regimes in valleys from climatological data available at relatively few locations: Frobisher Bay (Nawri and Stewart, 2006), The Owens Valley (Zhong et al., 2008), and the St. Lawrence River Valley (Carrera et al., 2009). However, the conceptual models of classic flows induced by topography may have limited skill in describing the complex flow structure and dynamics of the low-level winds resulting from various combinations of three-dimensional topography and meteorological conditions.

There are studies, based on high-resolution observational data and modelling, that revealed departures from the classic flows. Colle and Mass (2000) described a gap flow through the Strait of Juan de Fuca that was found to deviate from the classic gap flow within a long channel. A cross-strait pressure-gradient force induced by lee troughing caused by a flow descending over the strait from southern Vancouver Island forced the gap flow to bend, impeding an antitriptic balance along the strait. Loescher et al. (2006) differentiate between classic barrier jets and 'hybrid' jets along the coast of the Gulf of Alaska. The former occur when the onshore low-level flow is blocked by the coastal topographic barrier, whereas the latter develop when offshore-directed flows exiting gaps in the same barrier are deflected to the right by the Coriolis force and then merge with a coastal barrier jet. A hybrid gap and downslope wind through mesoscale gaps in the Cascade Mountains and the blocking effect of the Olympic Mountains on the ensuing leeside winds were studied by Colle and Mass (1998a, 1998b. Another example is the local amplification of a downslope wind (Adriatic bora) due to gap-flow effects (Gohm et al., 2008; Grisogono and Belušic, 2006).

This paper describes a complex low-level flow structure and dynamics simulated in the Iqaluit region (in the eastern Canadian Arctic, Fig. 1) during 7–8 November 2006, when an intensifying surface cyclone passed over the Labrador Sea. During the event, a northwesterly channelled wind, initiated as a barrier jet, interacted with a northeasterly downslope wind; both winds exhibited a very strong dependence on the cyclone. We use hourly surface observations at Iqaluit and soundings from radiosondes launched at the same location approximately every three hours to validate the simulations obtained with a limited-area mesoscale numerical model (Global Environmental Multiscale-Limited Area Model; GEM-LAM 2.5 km). Aside from gaining insight into an event that is representative for high winds at Iqaluit, the purpose of our analysis is to present an example of the almost simultaneous development of channelled and downslope winds (advecting different air masses) caused by the passage of a cyclone, as well as their interaction.

The high latitudes in our region of interest favour strong stability in the lower atmosphere, and hence low-level blocking and decoupling of low-level flows from the flows aloft, as well as the geostrophic adjustment through the high values of the Coriolis parameter. All of these enhance the impact of topography on low-level winds. Such an impact is expected in other high-latitude regions, even for modest topography. For instance, the strong influence of local topography on the local climatology in the eastern Canadian Arctic, and the important role played by the generally stable boundary layer at high latitudes are emphasized in Hudson et al. (2001). Unfortunately, due to the sparsity of observations in the region, most observational studies at high latitudes have been local. However, this situation is likely to change as a result of increasing interest in Arctic weather and climatology. This is exemplified by the study by Samelson and Barbour (2008), who simulated pressure-driven channelled winds within Nares Strait (centred at 80°N) and argued for their role in mediating the control of large-scale atmospheric variability on the variability of sea ice and fresh water through the strait.

The remainder of this paper is organized as follows. The next section presents the topography of southern Baffin Island and previous work on low-level winds at Iqaluit. Section 3 briefly describes the synoptic situation and the observed data. Section 4 contains a description of the model. The results are presented, validated, and discussed in Section 5. Section 6 presents the main findings of a short sensitivity study, and Section 7 contains the conclusions of the study.

2 Topography and previous work on winds at Iqaluit

a *Topography*

Baffin Island, the largest island of the Canadian Arctic Archipelago, is separated from Greenland by Baffin Bay and Davis Strait on the northeast and from mainland Canada (Ungava/Labrador Peninsula) by Hudson Strait on the southwest. The southern part of the island and its topography, as it is represented by the mean height of our model, are depicted in Fig. 1. Visible are Meta Incognita Peninsula, Hall Peninsula, and Cumberland Peninsula; all have a northwest-southeast orientation and are dominated by mountainous terrain. Hall Peninsula is separated from Meta Incognita Peninsula and Cumberland Peninsula by Frobisher Bay and Cumberland Sound, respectively. The two bodies of water are large inlets of the Labrador Sea that extend more than 200 km northwest into the island. Near the head of Frobisher Bay and at the base of the southwest slopes of Hall Peninsula lies Iqaluit, the largest community on Baffin Island.

Of particular interest to our study are the continuous mountain ridges over Hall and Meta Incognita peninsulas, reaching maximum elevations of approximately 1050 and 750 m, respectively. They flank both Frobisher Bay and the valley (Sylvia Grinnell Valley) extending northwest from the head of the bay. Relatively steep topographic slopes are found on the east and northeast sides of the two peninsulas. As will be shown in Section 5, the northeast slopes of Meta Incognita Peninsula play a crucial role in the initiation and development of the wind channelling simulated over Frobisher Bay. Near the head of the bay, the contour lines of lower elevations (<350 m) turn to the north by about 30°, while those of higher elevation maintain their orientation parallel to the bay's axis; the slopes remain steep in both elevation ranges (Fig. 1). Orographic blocking of the simulated low-level flow and the subsequent channelling occur along these directions.

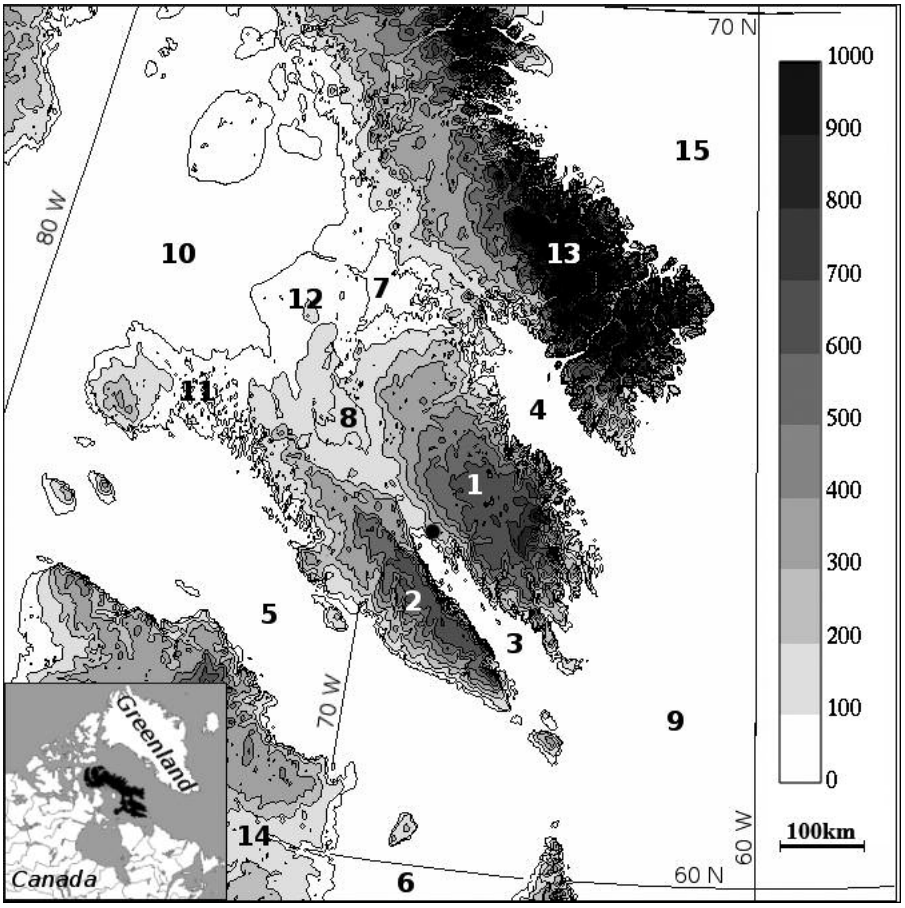

Fig. 1 Model domain and topography (m) over the southeast portion of Baffin Island. Only elevations less than 1000 m are represented, with a contour interval of 100 m. Geographical names: Hall Peninsula (1), Meta Incognita Peninsula (2), Frobisher Bay (3), Cumberland Sound (4), Hudson Strait (5), Ungava Bay (6), Nettilling Lake (7), Amadjuak Lake (8), Labrador Sea (9), Foxe Basin (10), Foxe Peninsula (11), The Great Plain of the Koukdjuak (12), Cumberland Peninsula (13), Ungava Peninsula (part of Labrador Peninsula) (14), and Davis Strait (15). The black dot near the head of Frobisher Bay marks Iqaluit's location. The insert in the lower left corner indicates the location of Baffin Island (shown in black).

b *Previous Work*

High wind events (HWEs) at Iqaluit, with surface wind speeds exceeding 15 m s^{-1}, occur mainly between October and March. The winds blow from three primary directions, 50–70°, 130–140°, and 310–350° mainly because of topographical effects on the broader synoptic flow. The overall frequency of occurrence (i.e., compared to all wind speeds and directions) of strong (>15 m s^{-1}) northwest, southeast, and northeast wind events are 2%, 0.2%, and 0.3%, respectively. This is equivalent to taking place on 3.6 days per winter from the northwest, once every third winter from the southeast, and once every second winter from the northeast. Northeasterly HWEs do not occur regularly; however, when they do occur, their impact on the community can, in some cases, be destructive (e.g., Hanesiak et al., 2010), hence their importance. Depending on the synoptic setting, a sharp transition from strong northeasterly to strong northwesterly winds typically ensues in less than one hour on many occasions and not all similar synoptic storm events generate strong northeasterly winds at the surface in Iqaluit (Prairie and Arctic Storm Prediction Centre (PASPC), personal communication, 2009). This makes forecasting strong northeasterly wind events as well as the timing of the transition to a northwesterly flow extremely challenging. Therefore, there is a need to understand better the physical processes that control these types of events. As will be shown in this paper, the underlying physics of these events is common around the globe, hence, a better understanding of these physical processes in this region of the Arctic can be applied to many other regions.

Hudson et al. (2001) noted the alignment of the prevailing surface winds at Iqaluit with the northwest-southeast axis of Frobisher Bay (Fig. 1), and they attributed the dominance of the strong northwesterly and north-northwesterly surface winds in winter to topographically induced wind channelling. In agreement with Hudson et al. (2001), the analysis of surface winds recorded at Iqaluit over a 21-year period (1985–2005) performed by Nawri and Stewart (2006) revealed that the northwesterly and southeasterly surface winds together accounted for more than 80% of all hourly observations of strong surface winds (>10 m s^{-1}). The highest

occurrence of strong winds was in October–March. The authors argued that the large-scale pressure field and downward turbulent momentum transfer from the overlying wind were the main external forcing mechanisms responsible for the prevailing surface winds at Iqaluit. Moreover, Nawri and Stewart (2008) found that cyclones provided conditions, through the associated large-scale pressure field, for both sustained and strong surface winds at Iqaluit along either the northwest or southeast direction and sudden shifts between these prevailing directions.

Nawri and Stewart (2006) also investigated the vertical structure of winds with surface speeds greater than 10 m s^{-1} using operational 12 h soundings at Iqaluit. The mean vertical profiles corresponding to northwesterly surface winds during the winter (January–March) showed an orographic low-level jet reaching its maximum speed at the surface. The term orographic was used to reflect the influence of the large-scale surrounding orography on the jet flow within the valley. The jet speed decreased monotonically with height within a layer characterized by a temperature inversion and reached a minimum value near the top of the inversion.

Nadeau (2007) analyzed the climatological conditions associated with strong surface winds at Iqaluit over the period January 1979 – March 2007. The focus was on HWEs, which were defined as winds with hourly surface speeds greater than 10 m s^{-1} for longer than three hours. In line with the studies mentioned previously, a dominant northwesterly wind regime with a frequency of 66.8% characterized these events. The five most severe of the northwesterly HWEs occurred in the cold season (October–April) and had surface winds with maximum speeds greater than 20 m s^{-1} oriented nearly perpendicular to the isobars of the synoptic-scale sea-level pressure. Nadeau (2007) considered this last feature indicative of pressure-driven channelling brought about by the presence of deep cyclones over the Labrador Sea. The mean atmospheric profile was also calculated for the five events at their peak intensity using data from the North American Regional Reanalysis. The profile shows a strong temperature inversion above the ridge level (considered at about 920 hPa) topping a boundary layer that is near-neutral below about 940 hPa. Because of this inversion, downward turbulent momentum transfer was ruled out as a principal contributor to the channelled wind. Interestingly, the mean profile revealed a low-level jet with a maximum speed at 900 hPa, which is different from the surface-intensified jet found by Nawri and Stewart (2006). Note, however, that the winter season in Nawri and Stewart (2006) is much shorter than the cold season in Nadeau (2007).

During the 7–8 November 2006 wind event addressed in this paper, the surface wind observed at Iqaluit became northwesterly and then maintained a speed greater than 10 m s^{-1} (19.4 kt) for longer than three hours. Therefore, the event can be classified as a northwesterly HWE, according to the definition of Nadeau (2007) and may be representative for its category.

3 Synoptic situation and data

a *Synoptic Situation*

Excerpts from the US 3-hourly Hydrometeorological Prediction Center (HPC) surface analysis charts covering southern Baffin Island and valid from 12:00 UTC, 7 November 2006 to 03:00 UTC on the next day are shown in Fig. 2. They reveal a low pressure system that moves northeastward over Ungava Bay and then intensifies over the Labrador Sea, while its centre remains offshore of southern Baffin Island. The 6-hourly National Centers for Environmental Prediction (NCEP) reanalysis data show an upper-level long-wave trough associated with the surface low over the same period of time. Figure 3 illustrates, for instance, the situation at 18:00 UTC, 7 November 2006. The change in direction of the wind near 500 hPa from southwesterly to westerly seen in the wind profiles from the radiosondes launched at Iqaluit between 14:31 UTC, 7 November 2006 and 02:15 UTC the next day (Fig. 4) is brought about by the passage of the upper-level trough over southern Baffin Island.

b *Surface Data and Soundings*

The surface data used in this paper consist of hourly observations of the 10 m wind speed and direction (2 min averages), 1.5 m temperature and dewpoint, and sea level pressure (all instantaneous values). The data were obtained from meteorological aviation reports (METARs) for the Iqaluit airport. Radiosondes launched at the same location at 14:31, 16:50, 20:15 and 23:20 UTC on 7 November 2006 and at 02:15 UTC the next day provided the upper-air data. Potential temperature and specific humidity were calculated from the observed data for comparison with the model results. Hereinafter, the 10 m wind and the 1.5 m temperature and dewpoint are referred to as the surface wind, surface temperature, and surface dewpoint, respectively.

4 Model description

To produce the simulations presented in this paper we ran the GEM-LAM with a horizontal resolution of approximately 2.5 km (Erfani et al., 2006). The model has been run in experimental operational mode at the Canadian Meteorological Centre (CMC) since 2006 over four windows covering different parts of Canada. The model is non-hydrostatic and uses a semi-implicit, semi-Lagrangian time integration. There are 58 vertical sigma-pressure hybrid coordinate levels up to 10 hPa. The physical parameterizations used include a unified cloudiness-turbulence scheme for the planetary boundary layer (MoisTKE; Belair et al., 2005), a radiation scheme (Garand and Mailhot, 1990; Fouquart and Bonnel, 1980), a shallow convection scheme (Kuo-Transient; Belair et al., 2005), and an explicit micro-physical condensation scheme (Kong and Yau, 1997) with no deep convection parameterization. The model's surface component uses a mosaic approach with four surface types: land, open water, sea ice, and glaciers. More details can be found in Erfani et al. (2006) and references therein.

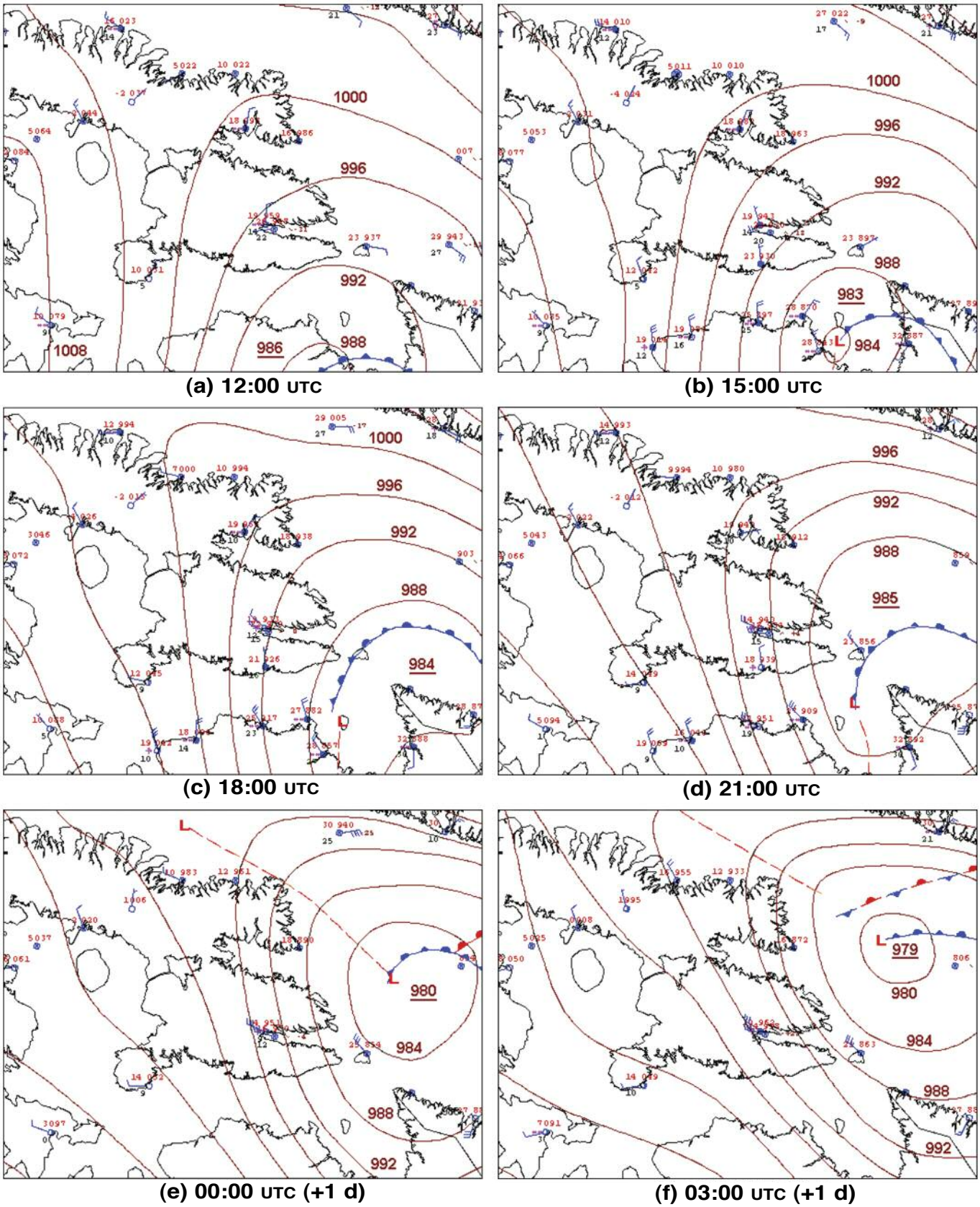

Fig. 2 HPC surface analyses valid at (a) 12:00, (b) 15:00, (c) 18:00, and (d) 21:00 UTC, 7 November 2006 and at (e) 00:00 and (f) 03:00 UTC on the next day (full barb = 10 knots).

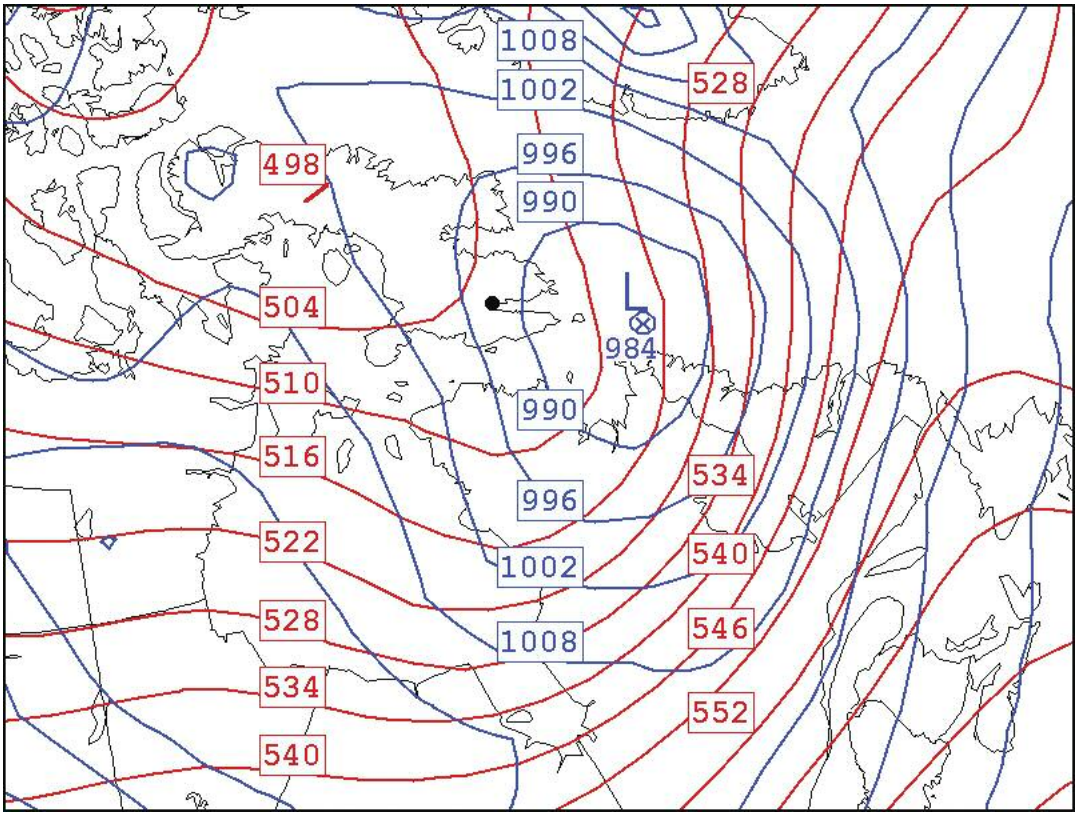

Fig. 3 Geopotential height at 500 hPa (red lines, contour interval 6 dam) and sea level pressure (blue lines, contour interval 6 hPa) at 18:00 UTC, 7 November 2006 from the NCEP reanalysis. The black dot near the head of Frobisher Bay marks Iqaluit's location.

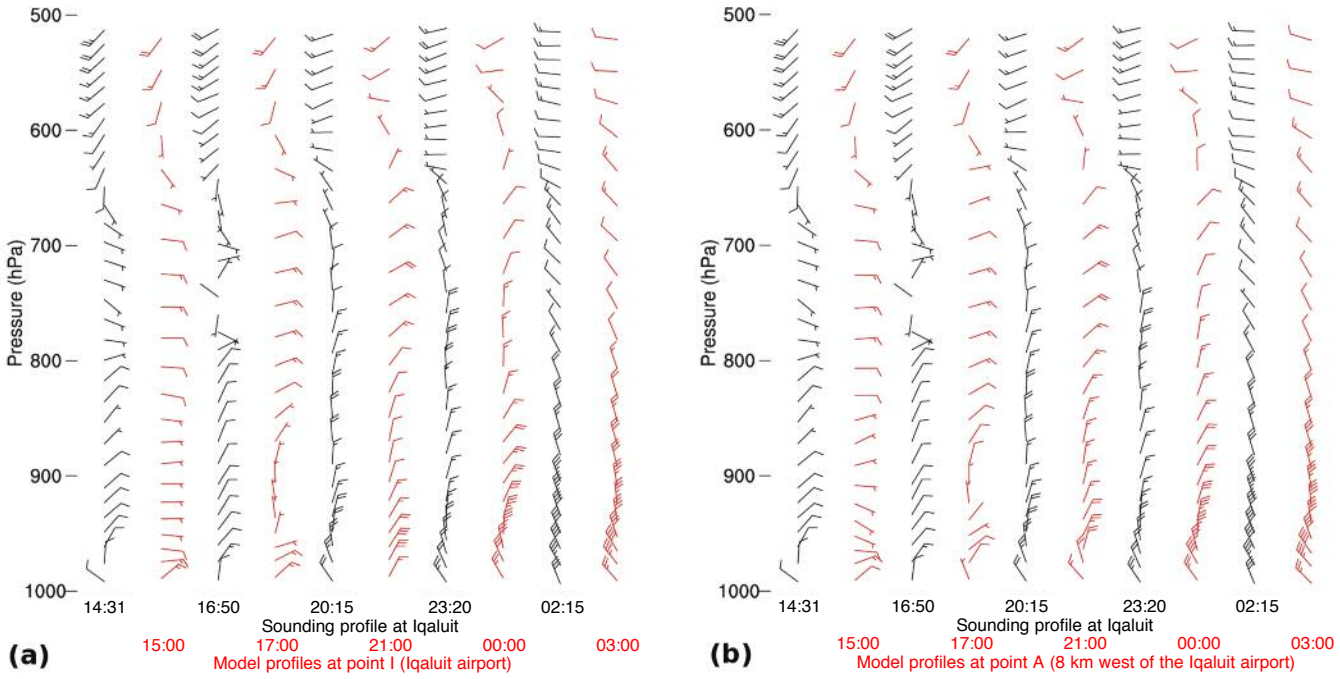

Fig. 4 Simulated wind profiles (red barbs) at points I (a) and A (b). The observed wind profiles from radiosondes launched at the Iqaluit airport (at the times given in the top row) are shown in black. All times are in UTC. A full barb is 10 knots.

We started with a model configuration similar to the configuration used at CMC for their window covering southern Baffin Island. The domain of our model is shown in Fig. 1, and its horizontal grid size is 480 × 480. We tested three novel features with respect to the aforementioned configuration. The first was a slightly modified version of the scheme proposed by Beljaars et al. (2004) for the vertical distribution of the turbulent form drag induced by the unresolved small-scale orography with horizontal scales up to 5 km. The second was a modified version of the Lenderink-Holtslag turbulent mixing length (Mailhot and Lock, 2004), and the third had an increased vertical resolution near the surface. Thus, six more levels were added to the two levels normally used in the GEM-LAM in the first 150 m above the surface. As a result, the thickness of the model's surface layer was reduced from approximately 40 m to 8 m. The increased vertical grid spacing near the surface should provide a better representation of the shallow stable boundary layers that commonly form at high latitudes. The sensitivity of the model to various combinations of these features is presented in Section 6, whereas the simulation investigated in the next section was obtained in an experiment (named HBL) using all of the features.

The model was integrated for 19 hours starting at 11:00 UTC, 7 November 2006 with a time step of 45 s. The initial and boundary conditions were extracted from the hourly output of the GEM Regional model, which was started at 06:00 UTC, 7 November 2006 with initial conditions from the global forecasting system of the CMC and integrated for 48 hours. This last model has a global non-uniform horizontal grid, with the highest resolution (15 km) in a central window covering North America (Mailhot et al., 2006).

5 Model results and validation

a *Wind Channelling*

The evolution of the simulated sea level pressure and surface wind from 12:00 UTC, 7 November 2006 to 03:00 UTC the next day is illustrated in Fig. 5. Of note is the low-level blocking of the strengthening onshore flow associated with this system. This occurs during the first few hours along the eastern and southeastern shores of Hall and Cumberland peninsulas (Figs 5a, 5b, and 5c), respectively, both being characterized by high and steep coastal topography.

The presence of the surface cyclone just south of Baffin Island at 16:35 UTC, 7 November 2006 is captured on the National Oceanic and Atmospheric Administration's (NOAA) infrared satellite image valid at that time (Fig. 6a). The northeast-southwest oriented cloud streets over northern Hudson Strait visible in this image were very likely generated by a low-level wind that blew off Foxe Peninsula and advected cold air over warmer open water. The surface wind recorded at stations located on both shores of northern Hudson Strait support the existence of a low-level northeasterly wind accelerating across the strait (Fig. 2b). Such a cold-air outbreak associated with a similar northeasterly low-level wind is simulated by the model during the first few hours after the start (Figs 5a, 5b, and 5c). A snapshot of the surface potential temperature and wind at 16:00 UTC is shown in Fig. 6b. The northeasterly wind blows over the Great Plain of the Koukdjuak, Nettilling Lake, and Amadjuak Lake (Fig. 1) carrying cold air originating from the slopes of northern Cumberland Peninsula all the way to Hudson Strait. The convective mixing occurring over the two ice-free lakes warms the air transiting the respective regions. Nonetheless, the low-level flow becomes statically stable again downstream of the lakes and thus prone to low-level blocking and lateral deflection caused by the relatively low altitude orography encountered along its path, as will be shown later. In the next three subsections, we describe the early and mature stages of the simulated wind channelling over Frobisher Bay and discuss the simulated and observed surface wind at Iqaluit.

1 EARLY STAGE

Since our investigation is concerned with wind channelling over Frobisher Bay, we focus our attention on the mesoscale structure of the low-level flow in the region. Figure 7 shows a close-up of the model topography in the vicinity of the head of Frobisher Bay. Superimposed are the simulated surface potential temperature, wind, and sea level pressure at different times. Low-level blocking occurs when the above-mentioned northeasterly wind reaches the northeastern slope of the gapless mountain ridge on the Meta Incognita Peninsula. The associated low wind speed regions are visible in Figs 7a and 8b, in which areas of calm winds (< 3 kt) are marked by circles. Cold air of the same origin as the air advected by the northeasterly wind, which penetrated the low-lying areas earlier, can also be seen along the same slope as it abruptly changes its direction by about 45° to border Sylvia Grinnell Valley. Vertical sections (Fig. 8c) show shallow wedge-shaped layers of cold air that are trapped against this steep slope as the relatively weak impinging wind fails to push this stable air over the mountain barrier, thus becoming partially blocked. Consequently, mesoscale shallow high pressure areas are generated and the resulting mesoscale pressure ridge in the sea level pressure isobar pattern can be seen in Fig. 7a. The near-surface impinging flow that comes down the slopes of Hall Peninsula first decelerates over the Sylvia Grinnell Valley and then rides up the wedge of cold air.

In the first stage, the low-level horizontal pressure gradient force (PGF) brought about by the pressure ridge, having a component induced by the large-scale pressure field and one by the mesoscale pressure perturbation, acts on almost stagnant trapped cold air. Therefore, the PGF is not balanced by the Coriolis and friction forces and it starts accelerating the air. The developing flow is simultaneously deflected by the Coriolis force and it eventully aligns with the mountain barrier. Once this stage is reached, the PGF has a cross-barrier component balanced by the Coriolis force, thus establishing a mesoscale geostrophic balance in that direction and an along-barrier component partially balanced by the friction force. This is reflected in the orientation of the surface pressure isobars at an angle to the barrier in Fig. 7. Note that similar low-level blocking and airflow acceleration occur almost

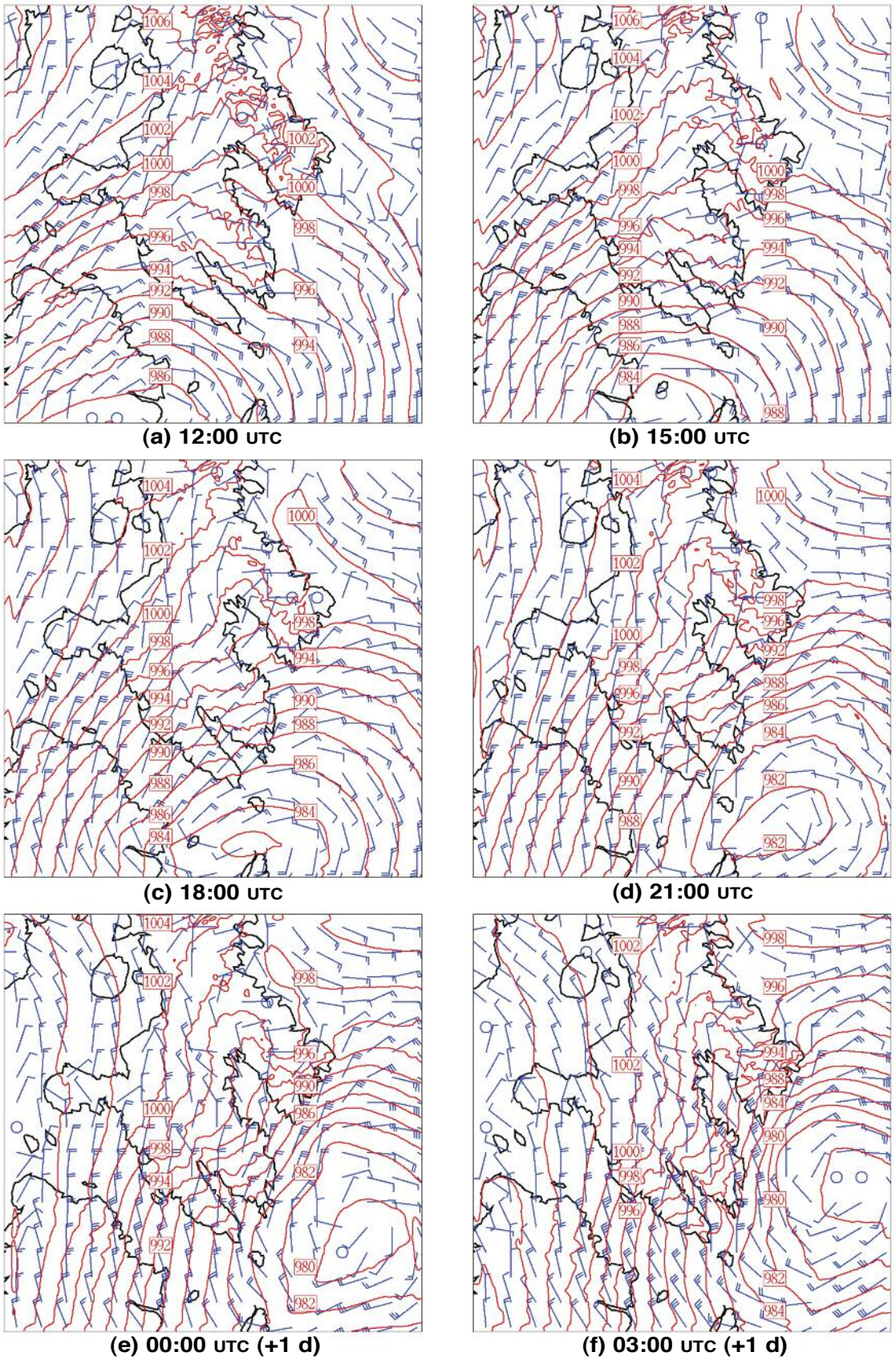

Fig. 5 Snapshots of the sea-level pressure (red lines, labelled values in hPa) and surface wind barbs (full barb = 10 knots) in the model simulation (HBL) investigated in the results section at (a) 12:00, (b) 15:00, (c) 18:00, (d) 21:00 UTC, 7 November 2006, and (e) 00:00 and (f) 03:00 UTC the next day. The open circles denote calm winds. Coastlines are shown in black.

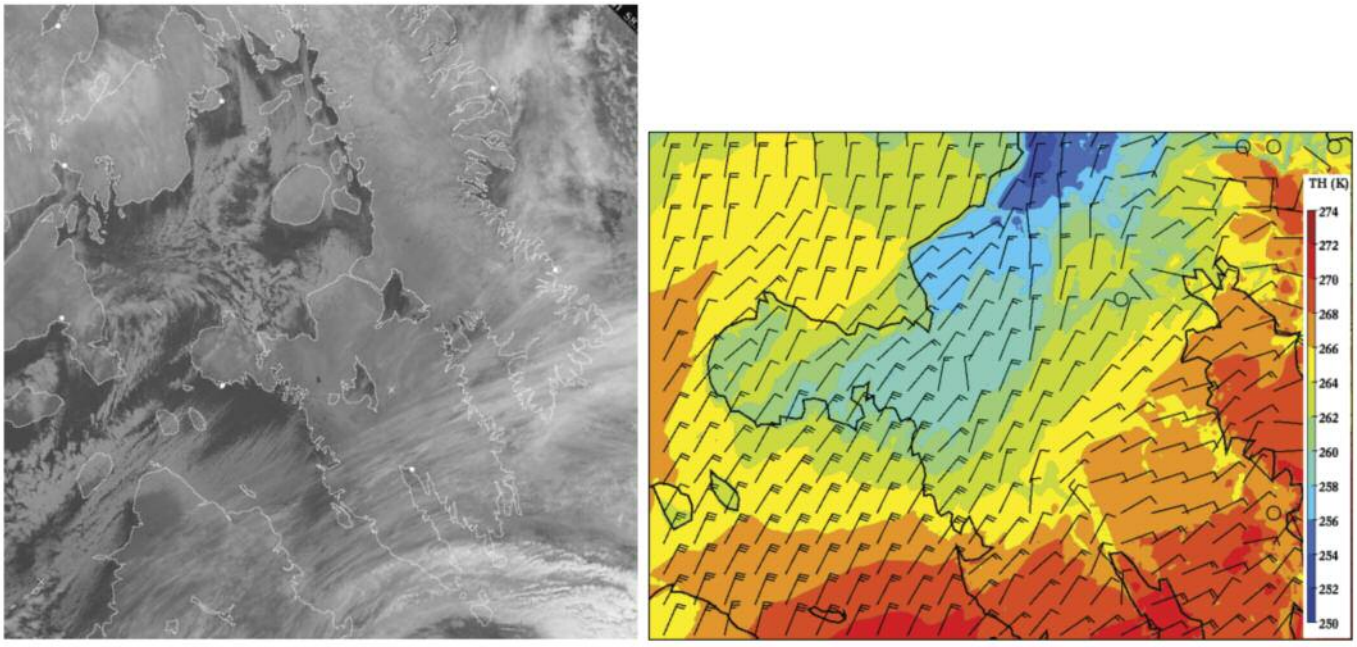

Fig. 6 a) Infrared satellite image valid at 16:35 UTC, 7 November 2006 (reproduced by permission of NOAA; image courtesy of Ron Goodson, Environment Canada). b) Simulated potential temperature at 1.5 m above the surface and surface wind barbs (full barb = 10 knots) at 16:00 UTC on the same day.

simultaneously along the steep upper-level slope located to the southwest of the lower-level slope mentioned earlier (Fig. 7a). The entrenchment of the cold air along the slope and the developing along-barrier wind resemble cold air damming and the associated barrier jet, respectively (Bell and Bossart, 1988; Whiteman,2000). The initiation of the barrier jet marks the onset of wind channelling in our simulation.

The near-surface along-barrier wind and the associated cold air advection, as well as the pressure ridge, progress along both the upper-level and lower-level slopes until these slopes merge. By 15:00 UTC the two flows have also merged (Fig. 7b), and the resulting barrier jet advances along the steep slope that is now facing Frobisher Bay. The air carried by the barrier jet over the bay experiences convective mixing and becomes warmer, and this can be seen in the downstream increase in the surface potential temperature. However, there remains a temperature contrast between the air advected by the barrier jet and the warmer air over the adjacent region of the bay, and this helps to maintain the mesoscale pressure ridge.

2 MATURE STAGE

Over the next several hours, the barrier jet advances even further along the mountain barrier and expands laterally across Sylvia Grinnell Valley and Frobisher Bay (Figs 7c, 7d, 7e, and 7f). The jet acts as an orographic barrier for the downslope wind over Hall Peninsula, which carries warmer and hence lighter air. The downslope wind decelerates as it approaches the jet and eventually overruns it. The decelerated flow creates a boundary region separating the two winds near the surface, which can be seen in the cross-sections shown in Figs 9b and 9d. The blocked air in this region starts to accelerate down the channel under the action of the local PGF and subsequently hugs the already developed colder channelled flow as a result of the Coriolis effect, thus generating its own barrier flow. This explains the lateral growth of the channelled wind region across Frobisher Bay. The ensuing widening of the channelled flow causes the downslope flow to decelerate and separate from the surface earlier (closer to the slope), and this leads to the propagation of the above-mentioned boundary toward the slopes of Hall Peninsula.

Downward transfer of momentum, forced, pressure-driven, and thermally driven channelling are all well-known mechanisms for wind channelling (Whiteman, 2000), and one or more of these could be at work at the same time. To identify the dominant mechanisms in our case, we first look at the relationship between the above-ridge winds and the near-surface channelled wind (Whiteman and Doran, 1993). The wind on the 850 hPa surface (above the ridge level) seen in Figs 10c, 10d, and 10e has a cross-mountain orientation that lends no support to the idea that the large scale flow could simply be diverted by the mountain barrier down the bay (forced channelling), or that there could be a downward transfer of momentum from the above-ridge flow large enough to drive the flow within the valley. Hence, neither can be a dominant mechanism for wind channelling before 00:00 UTC. The same figures also show the 850 hPa height contours becoming more closely spaced in time, while remaining almost perpendicular to the bay's axis. These features imply an increasing along-bay component of the large-scale pressure gradient over the same period of time. Therefore,

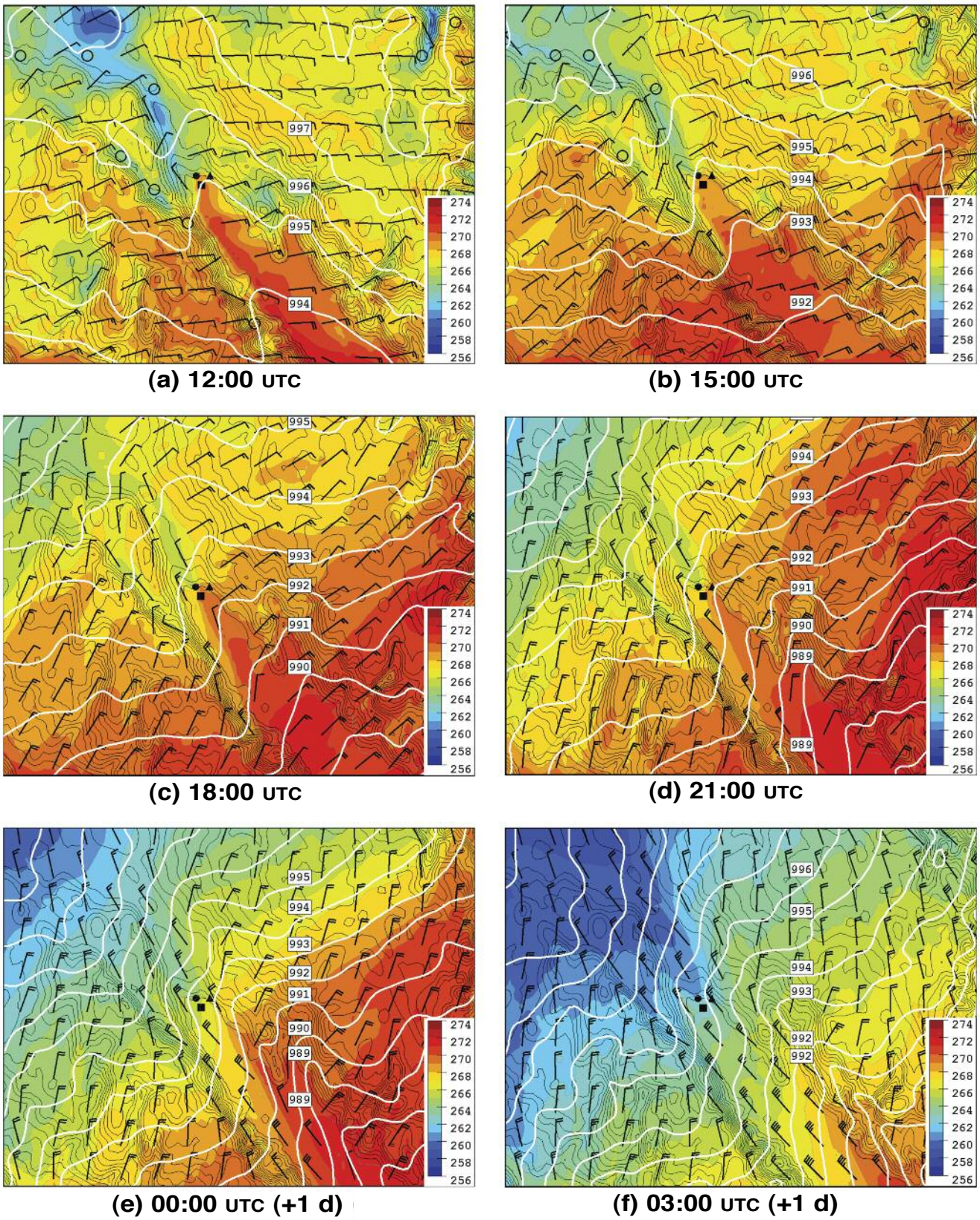

Fig. 7 Simulated potential temperature at 1.5 m above the surface (K, in colour), surface wind barbs (full barb = 10 knots) and sea-level pressure (thick white contours, labelled values in hPa) in HBL at (a) 12:00, (b) 15:00, (c) 18:00, (d) 21:00 UTC, 7 November 2006, and (e) 00:00 and (f) 03:00 UTC on the next day. Calm winds are denoted by open circles. The local topography is represented by contours (thin continuous black lines) every 50 m. The filled triangle, circle and rectangle mark the locations of points I (Iqaluit), A and B, in this order.

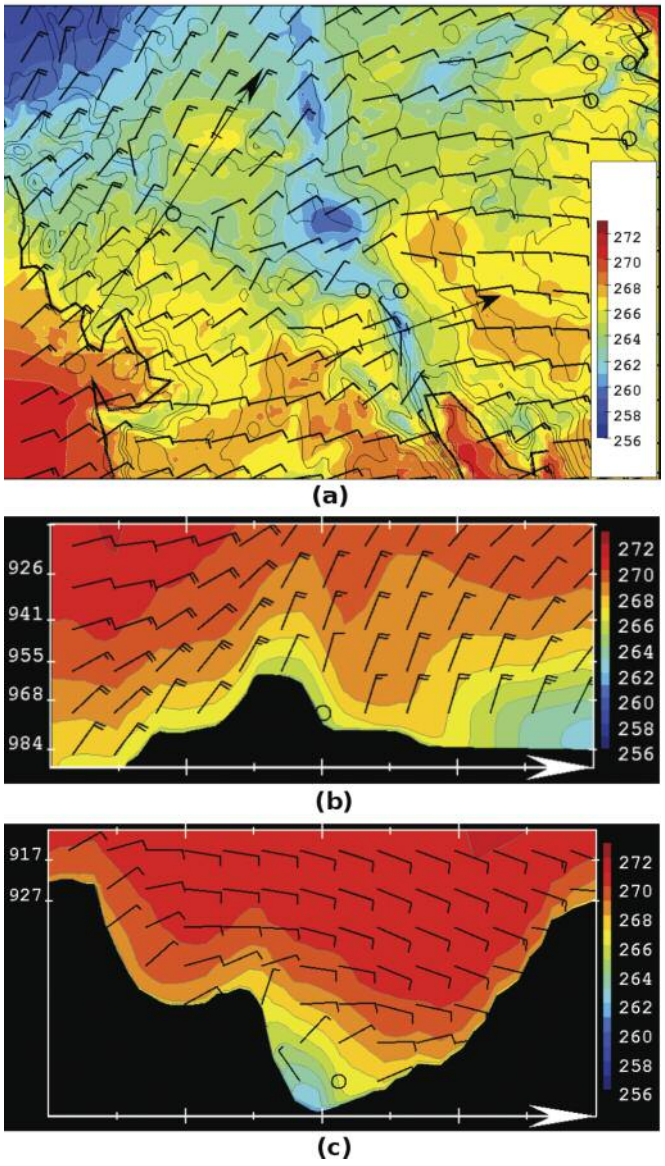

Fig. 8 (a) Simulated potential temperature at 1.5 m (colour, K) and surface wind barbs at 12:00 UTC, 7 November 2006. The thin black lines are topography isopleths (every 100 m), whereas the thick black lines are coastlines. The two arrows indicate the direction and horizontal extent of two cross-sections: Cross-section 1 (the arrow on the left) and Cross section 2 (the shorter arrow on the right). Potential temperature (colour, K) and horizontal wind barbs in Cross-section 1 (b) and 2 (c). The vertical axis extends from 910 to 990 hPa in Cross-section 1 and from 910 to 980 hPa in Cross-section 2. Calm winds are denoted by open circles and a full barb is 10 knots.

pressure-driven channelling (Whiteman and Dorran, 1993; Whiteman, 2000) is expected to play a major role in the development of the channelled wind following its initiation as a barrier jet.

A tongue of cold air associated with the channelled wind that precedes a larger scale southeastward low-level advection of cold air over the Hall and Meta Incognita peninsulas is clearly visible in Figs 7c, 7d, and 7e. The low-level horizontal temperature gradient along the bay strengthens with time and is equivalent to an increasing along-bay thermally induced pressure gradient. Consequently, the contribution of the thermally driven channelling should also increase. We can therefore conclude that wind channelling is mainly pressure and thermally driven during its mature stage.

The contribution of forced channelling should increase after 00:00 UTC as the large-scale flow aloft becomes northerly (Fig. 10f). Notice, for example, the surface wind northwest of the Sylvia Grinnell Valley (Fig. 7f) that becomes funnelled through this valley. Therefore, the big picture that emerges is that the mesoscale pressure gradient generated by low-level blocking and cold-air drainage into Sylvia Grinnell Valley triggers and initiates wind channelling through the generation of a barrier jet. Afterwards, both the large-scale pressure gradient and the thermally induced pressure gradient force the channelled wind in its mature stage. Forced channelling makes a minor contribution during this stage, but this is expected to increase after 00:00 UTC when the large-scale flow aloft changes its orientation and starts to have a stronger along-bay component. The transition from the initial to the mature stage is gradual for the case investigated herein.

3 THE SURFACE WIND AT IQALUIT

We first validate the model simulation against surface observations by comparing the simulated time series of the main surface variables extracted at three grid points to those observed at Iqaluit airport. One of the grid points, point I, is located at the airport, which is very close to the bay (< 2 km). The other two grid points, denoted by A and B, are approximately 8 km (three grid points) to the west and southwest of I, respectively (Fig. 7). Note that the averaging of the values at point I along with the values at the surrounding grid points has been avoided. One of the main reasons for doing so is the existence of strong surface flux gradients and even of a change in the static stability regime from stable over land to unstable over water near point I, due to its proximity to the bay. Another reason is the effect of the local orographic slope on the downslope wind and later on the channelled wind, once the latter has reached this slope.

Let us begin by analyzing the simulated time series. The surface wind at points I, A, and B (Figs 11a and 11d) is east-northeasterly during the first few hours (11:00–14:00 UTC), when the wind is downslope at point I and an extension of the same downslope wind at points A and B (Fig. 7a). By 23:00 UTC, all of the three points are in the channelled wind region, and the wind is northwesterly afterwards (Fig. 7e). Before 23:00 UTC, the boundary between the channelled and downslope wind (discussed in the previous section) propagated across the bay and caused the surface wind to change its direction gradually from east-northeasterly to northwesterly at points A and B first and then at point I (Fig. 7). The strong similarity between the time series of the surface wind speed and direction at points A and B reflects the fact that these points are approximately on the same 'phase line' of the cross-bay propagation of the wind channelling. The deceleration of the downslope wind in the first phase of

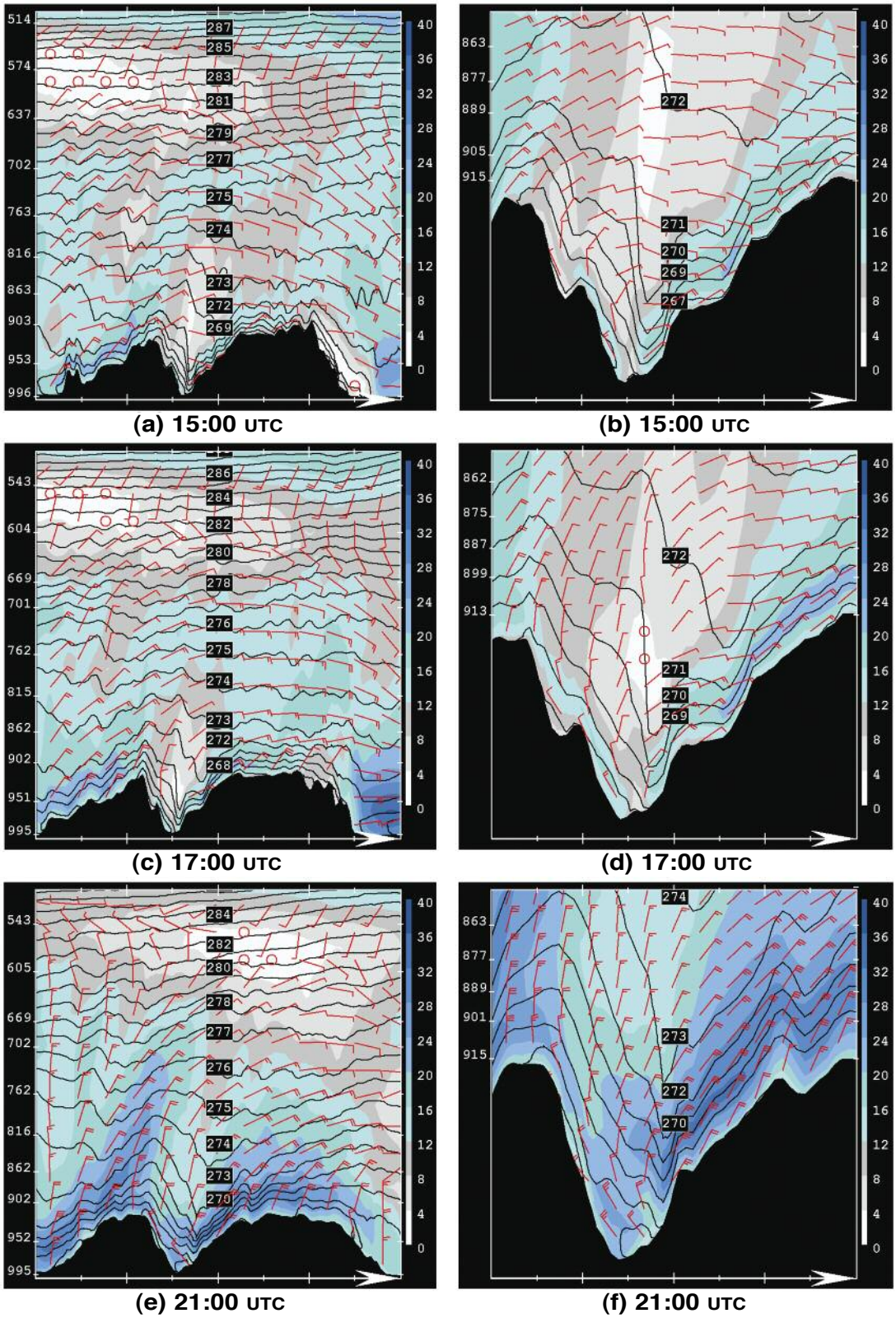

Fig. 9 Cross-sections through point A along lines that are approximately parallel to the 10 m wind simulated over the upper slopes of Hall Peninsula and upwind of point A at 15:00 UTC (top row), 17:00 UTC (middle row), and 21:00 UTC (bottom row). Isentropes (K, black contours) and wind barbs are superimposed on the wind speed field (knots, in colour). The sections in the left column encompass (from left to right) part of Hudson Strait, Meta Incognita Peninsula, and Sylvia Grinnell Valley (seen near the middle of the sections), Hall Peninsula and part of Cumberland Sound. Close-ups of these sections showing Sylvia Grinnell Valley and the slopes of Meta Incognita and Hall peninsulas facing this valley are shown in the right column. Point A is near the centre of Sylvia Grinnell Valley in the figures. The vertical axes extend from 1000 hPa to 500 hPa in the full sections and from 1000 hPa to 850 hPa in the close-ups. Open circles denote calm winds and a full barb is 10 knots.

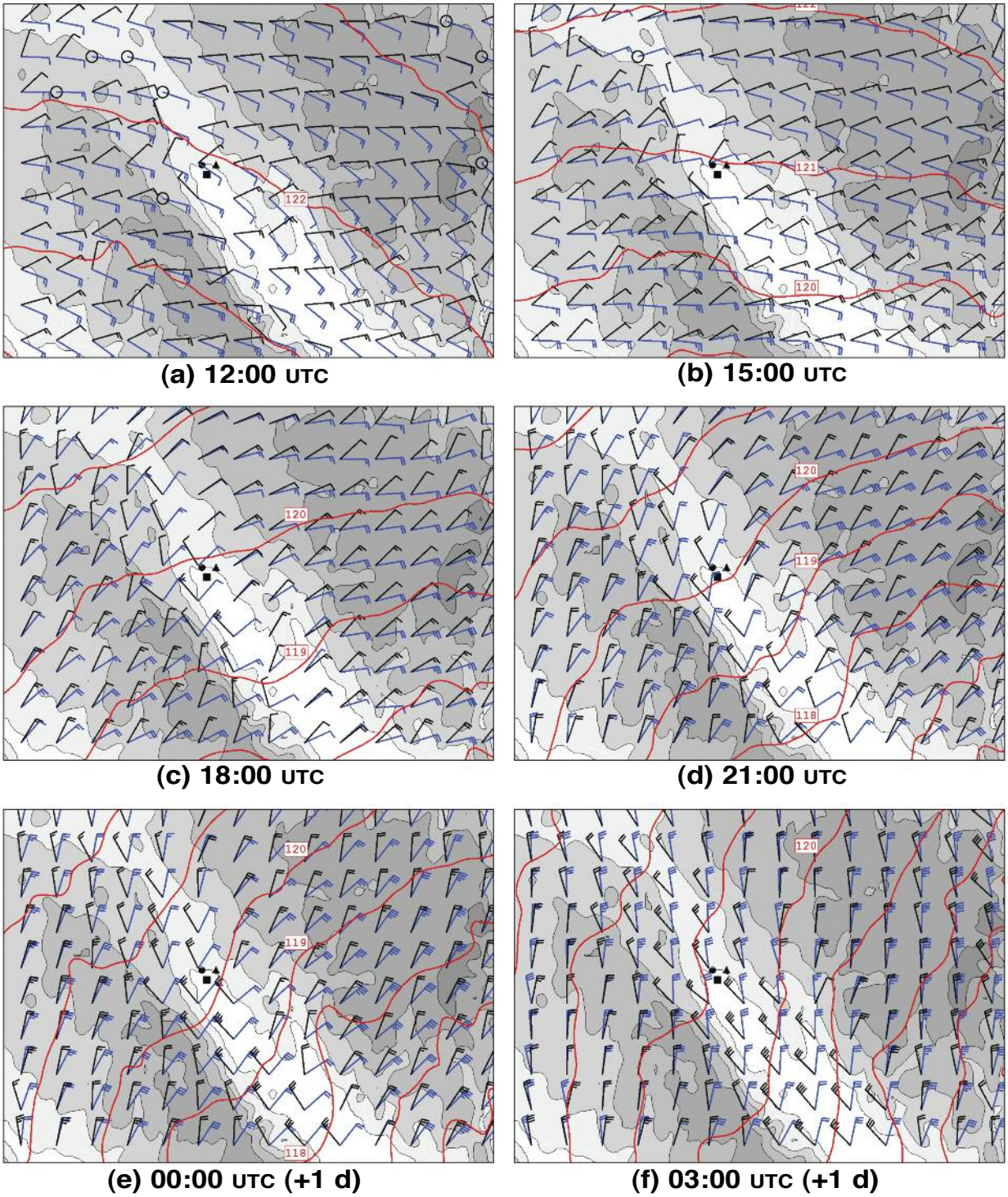

Fig. 10 Simulated surface wind barbs (black), 850 hPa wind barbs (blue), and geopotential height at 850 hPa (red contours, labelled values in decameters) in HBL at (a) 12:00, (b) 15:00, (c) 18:00, (d) 21:00 UTC, 7 November 2006, and (e) 00:00 and (f) 03:00 UTC on the next day. The region shown is the same as in Fig. 7. Calm winds are denoted by open circles. The topography is represented by the 15, 200, 400, 600, 800, and 1000 m contours (thin black lines). The filled triangle, circle and rectangle mark the locations of points I (Iqaluit), A, and B, respectively. A full barb is 10 knots.

the directional shift followed by an acceleration of the resulting weak wind, both taking place in the above-mentioned boundary region, explains why the wind speed drops and then increases at points A and B between 14:00 and 19:00 UTC. By 19:00 UTC, point A is in the channelled wind area and the wind direction maintains an almost northwesterly direction afterwards. The generally higher values of wind speed, temperature, and specific humidity at point B (bay point) compared to those at points A and I (land points) are the result of convective mixing occurring over water.

Interestingly, the simulated time series at point A are a much better match to the observations than those at point I (representing the weather station's location), especially the time series of the surface wind speed and direction (Fig. 11). Their close similarity to the observed time series supports the development of a channelled wind over Frobisher Bay during the 7–8 November 2006 wind event that had strong similarities to the simulated wind. The time series of the observed surface temperature and specific humidity (Figs 11b and 11c) show cooling and drying of the air at Iqaluit that reveal a change in air mass brought about by the channelled wind. The air carried by the downslope wind is warmer and more humid.

The poorer match obtained at point I can be attributed to many factors, the simulated downslope flow being an important one. As shall be seen in the next section, this flow is generated by a mountain wave whose accurate simulation is challenging. A downslope flow near Iqaluit that is stronger than the observed flow (see the profiles and the wind speed time series) may provide increased resistance to the cross-bay advancement of the channelled wind and could explain the delayed arrival of the latter at Iqaluit. Another factor could be the less accurate representation of the local topography by the filtered topography of the 2.5 km resolution model. For instance, the fine topographic features with north-northwest orientation that exist near Iqaluit (not shown) are missing and the valley of the Sylvia Grinnell River, which flows into the bay approximately 1 km to the west of Iqaluit is not resolved. These features could have a local, but significant effect on surface winds in the stable boundary layer, which is the case on land in the simulation. The fact that the results at point I are much less realistic than at point A provides an example of locally poor results, while the simulated mesoscale flow may be reasonably accurate. This result could be useful for forecasters.

b *Characteristics of the Simulated Mountain Waves and Their Interaction With the Channelled Wind*

Strong downslope winds (> 30 kt) associated with mountain waves develop in the simulation over the southwest slopes of Hall and Meta Incognita peninsulas. The waves are generated when the large-scale winds accompanying the surface cyclone impinge on the eastern slopes of Hall Peninsula. Such conditions, with unimpeded large-scale winds blowing towards the peninsula, last for more than 10 h, until about 00:00 UTC (Fig. 5). The situation is somewhat similar to that described by Fudeyasu et al. (2008), who identified a strong dependence of downslope winds on mountain waves generated by a surface cyclone on the cyclone's movement.

Vertical cross-sections of wind and potential temperature through point A that are approximately parallel to the surface wind over the upper-level lee slopes of Hall Peninsula and upwind of point A, at different times, are depicted in Fig. 9. With the isentropes giving an indication of the streamlines of the mountain wave flow, the sections show the development of a mountain wave over Hall Peninsula followed downstream by another over Meta Incognita Peninsula. Although the simulated mountain waves reach their maximum amplitudes further south where the mountains are higher and the slopes are steeper, some remarkable features are clearly illustrated in Fig. 9. One is the wave amplitude decay with height (reflected by the decreasing slopes of the isentropes) up to a level where the wind is either calm or becomes perpendicular to the near-surface wind over the slopes and thus acts as a mean-state critical level for mountain waves (e.g., Kim and Mahrt, 1992). This is indicative of wave absorption below a critical level induced by directional wind shear. Observational evidence of mountain wave absorption in such conditions is given in Worthington and Thomas (1996) and Doyle and Jiang (2006); the latter authors also present results from a numerical simulation of the phenomenon. Another feature is the strengthening of the simulated low-level winds on the lee slopes while the mountain waves are confined below the critical level and become essentially decoupled from the flow aloft.

Both features make the situation similar to the classic situation of mountain waves in the presence of critical levels that could generate strong downslope winds, with the bora windstorm being representative of this case (Durran, 2002; Gohm et al., 2008). Within the framework of hydraulic theory, the strengthening of the wind on the lee slope is explained by its similarity to the flow regime characterized by a supercritical flow accelerating down the slope as its potential energy is converted into kinetic energy (Durran, 2002); the change in flow regime from subcritical to supercritical takes place at the mountain top. Simulations of strong downslope winds brought about by mountain waves in the presence of a mean-state critical level that are supported by observations are presented in Gohm et al. (2008) and Fudeyasu et al. (2008).

A very interesting and important aspect of the simulated flow dynamics is the interaction of the downslope flow over Hall Peninsula with the channelled flow. The sections in Figs 9b, 9d, and 9f depict the development of the northwesterly channelled wind, reflected by an increase in speed and in vertical and horizontal extent, as well as the wedge of cold air associated with it. The boundary region of weak winds that separate the downslope wind from the channelled wind can also be seen in the same figures. A striking feature above the valley is the jump experienced by the downslope wind. Strong vertical motion and isentropes sloping steeply upward characterize the jump region, and convective mixing ensues when the isentropes overturn, that is, when wave breaking occurs. Unlike the classic hydraulic jump that occurs when an unimpeded supercritical downslope flow transitions to a subcritical regime downstream, an example of which is the jump associated with the strong bora wind reported by Gohm et al. (2008), the simulated jump is brought about by the existence of a flow coming from a different direction and advecting denser air. This flow acts almost like a topographic barrier in the path of the downslope flow carrying lighter air. Consequently, the downslope flow becomes an overrunning flow that contributes to the development of a mountain wave over Meta Incognita Peninsula right downstream of the jump, and this further complicates the local situation.

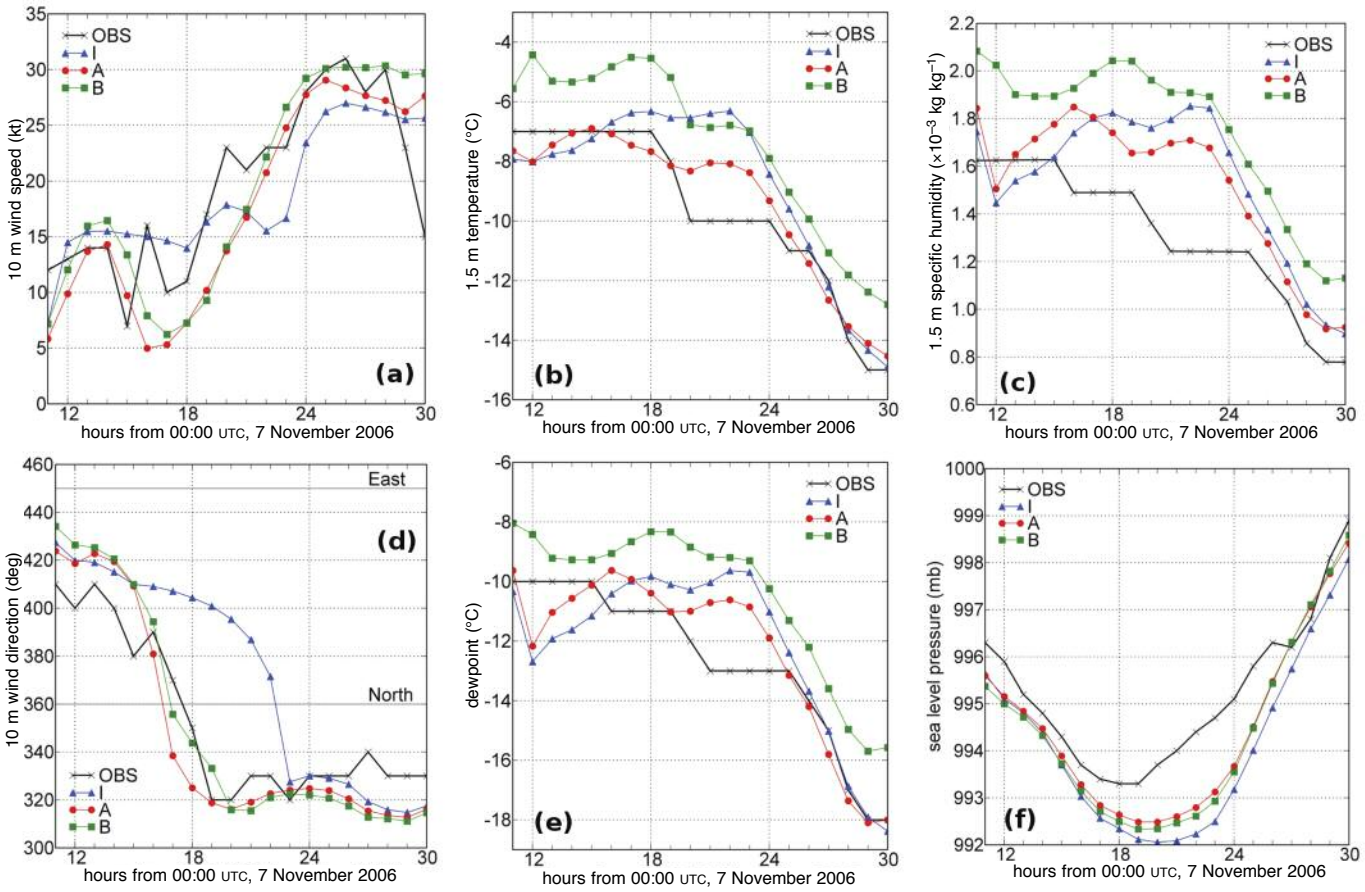

Fig. 11 Observed and model time series of (a) the 10 m wind speed, (b) the 1.5 m temperature, (c) the 1.5 m specific humidity, (d) the 10 m wind direction, (e) the dewpoint temperature, and (f) the sea level pressure. The observations were taken at Iqaluit airport, whereas the model data were obtained at points I, A, and B, in the HBL experiment.

c *Validation of the Simulated Flow and Stratification using Sounding Profiles*

We continue the validation of the model simulation started in Section 5a by comparing the simulated profiles to profiles from radiosondes launched at Iqaluit airport. Simulated vertical profiles of the wind speed and direction, potential temperature, and specific humidity at points I and A are plotted alongside (slanted) sounding profiles in Figs 12 and 4. The figures show a generally better fit of the profiles at point A to the soundings, which is consistent with the better fit obtained at the same point for the time series of the surface variables. Notice, for instance, the more realistic near-surface directional wind shear simulated at point A at 21:00 UTC, indicating the arrival of the northwesterly channelled flow at point A by that time. Note that the profiles simulated at point B have not been plotted because they are similar to those at point A above a boundary layer in which convective mixing occurs at point B only and more unrealistic within that layer.

1 VALIDATION WITH THE 14:31 AND 16:50 UTC SOUNDINGS

The two soundings reveal a relatively deep flow extending from 950 hPa up to about 800 hPa (Figs 12b, 12f, and 4, which is almost unidirectional from the northeast (hence downslope) and whose speed varies in a narrow speed range (Figs 12a and 12e). The wind weakens quite abruptly above 800 hPa, creating reverse wind shear. This is associated with strong directional shear, both occurring in a weakly stratified layer in the 14:31 UTC sounding (Fig.12c), and in a mixed layer in the 16:50 UTC sounding (Fig. 12g). Both wind profiles also reveal the presence of a mean-state critical level at about 680 hPa (Fig. 4).

All of these features point to the existence of a strengthening downslope flow brought about by a mountain wave trapped below a mean-state critical level. They also show that mixing occurs and intensifies at the top of the downslope flow until a mixed layer is created. The transition from a weakly stratified to a mixed layer is accompanied by a deceleration of the flow in the same layer. Notice that the flow becomes nearly stagnant (< 3 kt) from about 750 hPa up to the critical level (Fig. 12e). Thus, there is an indication of enhanced mixing and wave-induced drag accompanying the intensifying downslope flow. The mixing could be attributed to wave breaking or shear instability. For a discussion on which of the two mechanisms might be responsible for the generation of the mixed layer topping downslope flows the reader is referred to Gohm et al. (2008) and the references therein. Observational

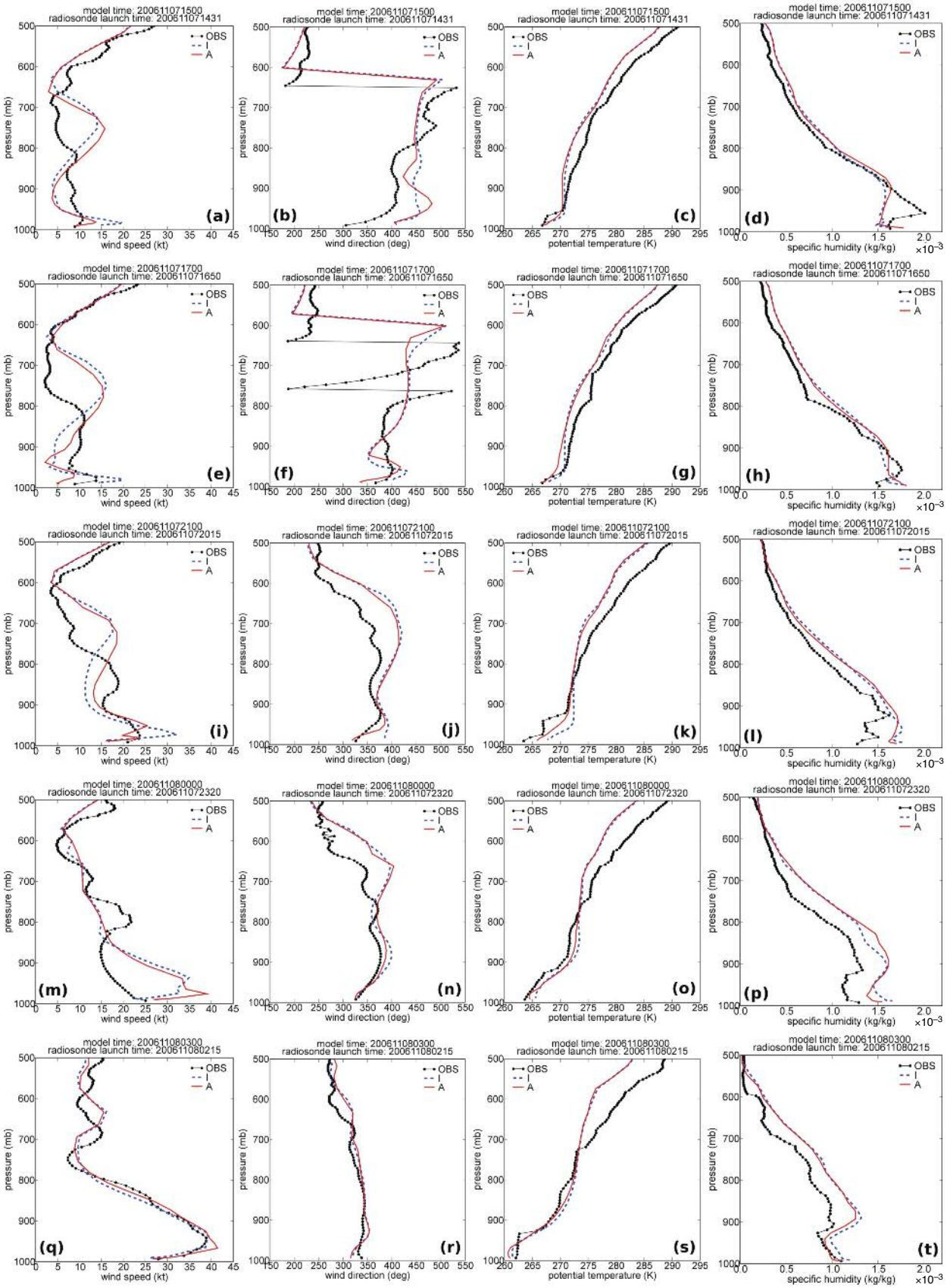

Fig. 12 Profiles of wind speed (first column), wind direction (second column), potential temperature (third column), specific humidity (fourth column) simulated at points I and A and obtained from radiosondes launched at Iqaluit airport. The model and radiosonde launching times are 15:00 UTC and 14:31 UTC, respectively (a–d), 17:00 UTC and 16:50 UTC (e–h), 21:00 UTC and 20:15 UTC (i–l), 00:00 UTC and 23:20 UTC (m–p), and 00:30 UTC and 02:15 UTC (q–t).

evidence of a strengthening downslope flow below a critical level, which is topped by a weakly stable layer characterized by an increasing reverse wind shear and directional shear that is associated with wave breaking is provided in Jiang and Doyle (2004, Fig 3).

A near-surface wind with a speed profile resembling that of a low-level jet can be seen developing below 950 hPa. It has a distinct temperature and moisture signature from the wind above (Figs 12c and 12d), from which it is separated by large gradients of the two quantities. These characteristics and the directional shear make the near-surface wind appear decoupled from the downslope wind aloft. One explanation might be that the channelled wind had reached Iqaluit by 14:31 UTC as a result of rapid cross-bay development. This might have been possible if the relatively weak downslope wind at that time provided little opposition to the lateral advancement of the channelled flow. The subsequent strengthening of the downslope wind would have pushed the channelled flow back and thus re-established a downslope flow reaching the surface at Iqaluit for at least one hour. This would explain the increase in the surface wind direction angle and speed seen in Figs 11d and 11a from 15:00 and 16:00 UTC. Such a back-and-forth movement of the channelled and downslope winds was simulated in two of the experiments mentioned in Section 6. The angle of the direction of the surface wind at point A in these experiments increases from 17:00 UTC to 19:00 UTC, after which it again starts to decrease.

The vertical profiles simulated at 15:00 UTC and 17:00 UTC at point A are now compared to the above-mentioned sounding profiles. The model simulates a mean-state critical level due to wind turning with height near 650 hPa at 15:00 UTC and near 620 hPa at 17:00 UTC (Fig. 4b), which is slightly higher than the observed critical height. Nonetheless, the model is not capable of simulating wave breaking or entrainment at the top of the downslope flow, leading to the generation of a mixed layer below the critical layer, in part, because of the model's rather coarse horizontal and vertical resolution. Notice, however, that the simulated wind is very weak (3 kt) in the vicinity of the critical level.

At 15:00 UTC, the low-level wind with a maximum speed of about 14 kt (Fig. 12a) is the downslope wind associated with the wave over Hall Peninsula, whereas the wind with a maximum speed of 15 kt near 750 hPa is associated with the mountain wave over Meta Incognita Peninsula (Figs 9a and 9b). The weaker wind, at 4 kt, near 920 hPa is the decelerated wind near the jump experienced by the downslope flow. Interestingly, the wind simulated at 17:00 UTC has a speed profile (Fig. 12e) nearly identical to that at 15:00 UTC between 500 and 900 hPa. Below 900 hPa, the low-level wind at point A weakens and changes its direction in the 2 h period mainly because of the cross-valley propagation of the channelled wind, which acts as a moving barrier for the downslope flow (Figs 9b and 9d). Notice that the observed low-level wind at 17:00 UTC (with a maximum speed of 14 kt) is stronger than the one simulated at point A (8 kt) and weaker than that simulated at point I (20 kt), this point being reached by the channelled wind later in time than at point A.

The similarity between the wind speed profile from the 16:50 UTC sounding and the one simulated at 17:00 UTC helps improve our interpretation of the former. Thus, the wind observed below 950 hPa appears to be induced by a downslope wind over Hall Peninsula that experiences something similar to a jump a short distance downstream. This would lead to the observed wind deceleration and near-neutral temperature profile (as a result of enhanced mixing) seen in the layer between 900 and 950 hPa in Figs 12e and 12g, respectively. It is also very likely that the wind between 800 and 900 hPa was associated with a mountain wave developing over Meta Incognita Peninsula. The confinement of this mountain wave to lower altitudes than the simulated wave could be, in part, due to the lower altitude of the observed critical level. It is interesting to note that the simulated profiles capture both mountain waves, and it is very likely that the radiosondes also sampled two similar waves.

2 VALIDATION WITH THE 20:15 UTC SOUNDING

The simulated channelled wind reached point A and the nearby slopes by 21:00 UTC (Figs 9f and 4b), thus forcing the downslope wind to separate from the surface and blow aloft before reaching the base of the slope. Both winds are captured by the wind speed profile simulated at point A at 21:00 UTC (Fig. 12i), in which the channelled wind has a maximum speed of 24 kt near the surface and the wind overrunning it has a maximum speed of 26 kt at about 950 hPa. Also captured, between about 800 hPa and 900 hPa, is the tongue of relatively weak wind that can be seen in Fig. 9e extending down from the critical level (existent near 580 hPa) and overlying the downslope flow over Hall Peninsula. The tongue separates this flow from the flow associated with the mountain wave that amplifies over Meta Incognita Peninsula. The speed of the latter increases with height to a maximum of 18 kt near 730 hPa in the profile shown in Fig. 12i, and then decreases to about 4 kt near the critical level (approximately 580 hPa).

The 20:15 UTC sounding reveals a flow pattern similar to that simulated at 21:00 UTC. The similarity of the observed and simulated wind speeds and direction below 900 hPa (Figs 12i and 12j) along with the temperature and humidity profiles (Figs 12k and 12l) provide support for the existence of a near-surface northwesterly flow advecting cold and dry air that was overrun by an almost equally strong northeasterly wind. The observed temperature and moisture profiles indicate strong mixing between the two flows, and this could explain the lack of strong speed gradients between the two winds. Such a situation would produce turbulence that could be particularly hazardous for airplanes landing and departing from Iqaluit airport. Hudson et al. (2001) mention occurrences of strong northeasterly winds blowing over weaker northwesterly surface winds at Iqaluit airport, and the potential of the resulting wind shear to generate severe low-level turbulence that is dangerous for aircraft.

As in the case of the 16:50 UTC sounding, the weakening of the wind in a nearly mixed layer near 900 hPa could be

attributed to the proximity of a jump experienced by the overrunning flow. Also, the pattern of the strong wind aloft (reaching 18 kt at 850 hPa) appears to be that of a wind induced by a mountain wave over Meta Incognita Peninsula, whose speed decreases with height up to a critical level. Such a level can be seen near 650 hPa in a directional wind shear layer in Fig. 4.

3 VALIDATION WITH THE 23:20 AND 02:15 UTC SOUNDINGS

The intensity of the simulated wind impinging on the northeastern slopes of Hall Peninsula starts decreasing prior to 00:00 UTC, as the cyclone continues to move northeast (Fig. 5). As a result, the cross-barrier wind weakens and eventually vanishes. Simultaneously, the low-level north-northwesterly wind blowing off the Great Plain of the Koukdjuak and Nettilling Lake gains an increasing influence on the downslope winds on both Hall and Meta Incognita peninsulas. This is illustrated by the tendency of these winds to become northerly in Figs 7e and 7f.

The wind profile simulated at point A at 00:00 UTC (Fig. 12m) shows a strong channelled wind with a maximum speed of 40 kt at 970 hPa overlaid by an overrunning wind with a maximum speed of 34 kt at 950 hPa. Although the mountain wave over Meta Incognita Peninsula is still simulated at this time, the induced flow no longer extends far enough upstream to appear in the wind profile at point A.

The wind direction and temperature profiles from the 23:20 UTC sounding are very close to those simulated at 00:00 UTC below 750 hPa (Figs 12n and 12o). Moreover, both the observed and simulated specific humidity profiles have a very similar pattern (Fig. 12p). However, the very different wind speed patterns and large differences in wind speed (reaching 18 kt near the surface) make the model validation challenging. One possible explanation of the monotonic increase in the observed wind speed towards the surface is that the overrunning flow experienced strong deceleration, possibly due to a jump, and that the deceleration was passed down to a strong channelled flow through turbulent mixing. Support for continuous mixing between the channelled flow and the overrunning flow is found by comparing the temperature and humidity profiles below 920 hPa from the 23:20 UTC sounding to those from the 20:15 UTC sounding. On the other hand, the relatively weak wind in a nearly mixed layer between 820 and 890 hPa points to the existence of a jump nearby. The strong wind observed between 740 and 820 hPa (Fig. 12m) could be due to a mountain wave over Meta Incognita Peninsula that was captured by the slanted sounding profile. Notice that a critical level still exists near 650 hPa (Fig. 4).

The wind speed and direction profiles from the 02:15 UTC sounding are simulated well by the model at 03:00 UTC, especially below 800 hPa (Figs 12q, 12r, and 4b). Noting that the ridge level in a cross-section through point A and perpendicular to the valley's axis is at approximately 910 hPa, both the observed and simulated channelled winds appear as well-developed low-level jets reaching their maximum speed below this level (Fig. 12q). The north-northwesterly direction of the simulated wind above the ridge level indicates an increasing contribution of forced channelling to the strength of the channelled wind. While the simulated turbulent mixing is strong below the jet nose, it is much reduced above it due to the presence of a temperature inversion (Figs 12s and 12t). Similarly, the occurrence of strong turbulent mixing explains the near-neutral temperature profile observed below the jet nose at 02:15 UTC, while suppressed mixing and hence limited turbulent momentum transfer are expected in the layer above, which is characterized by a strong temperature inversion (and high moisture gradient). Given the north-northwesterly direction of the observed near-surface wind (Fig. 12r), it is very likely that shortly after launch the radiosonde sampled the unstable boundary layer resulting from cold air advection over the open water of the bay, which would explain the enhanced mixing inferred from the sounding. Notice that the strong low-level mixing strengthens the temperature inversion by reducing the temperature at the base of the inversion.

The low-level jets observed at 02:15 UTC and simulated at 03:00 UTC bear a resemblance to those revealed by the mean atmospheric profile of Nadeau (2007) mentioned in the introduction. Recall, however, that the winds (mean jet) in Nadeau (2007) corresponds to stronger winds (with maximum speeds at the surface >38 kt). Therefore, stronger turbulent mixing might have occurred and this would contribute to the explanation of why this mean jet reaches a maximum speed at a higher elevation (approximately 900 hPa), which is above the ridge level.

6 Short sensitivity study

Several experiments were performed with different combinations of the novel features mentioned in Section 4, with the aim of investigating their potential for improving the simulations (Table 1). A control experiment (named CTRL), using the same effective roughness length approach, mixing length, and vertical resolution as the GEM-LAM 2.5 km used at CMC over the Baffin Island window, was also carried out. Since a comprehensive sensitivity study is beyond the scope of this paper, we only mention a few main findings here. The closest agreement with the observations at Iqaluit was obtained in the HBL run at point A. This can be seen, for example, in Fig. 13 which shows the time series of the surface wind speed and direction obtained at that point. Moreover, an overall better match to the observations was obtained at point A rather than at point I, in all experiments.

Most numerical weather prediction models (including GEM) use an effective (regional) roughness length obtained by enhancing the vegetative (local) roughness length with a component representing the small-scale unresolved orography. Its effect is an increased surface turbulent momentum flux, which leads to enhanced turbulent mixing in the boundary layer. This is supposed to mimic the combined turbulent drag induced by the vegetative cover and the unresolved small-scale orography (form drag). Beljaars et al. (2004) proposed an alternative to the effective roughness length

TABLE 1. The model experiments selected for the sensitivity study. The turbulent mixing length of Blackadar (1962) and the Lenderink-Holtslag modified mixing length proposed by Mailhot and Lock (2004), denoted by blac62 and lhm, respectively, were tested. A slightly modified version of the distributed drag scheme of Beljaars et al. (2004), denoted by belj04, was used in three experiments.

	CTRL	BELJ	LHM	BJLH	HBL
Distributed drag	—	belj04	—	belj04	belj04
Mixing length	blac62	blac62	lhm	lhm	lhm
Increased vertical resolution	no	no	no	no	yes

approach. They provide a parametrization for the turbulent form drag due to the sub-grid orography with horizontal scales <5 km, by explicitly distributing it vertically. Having separated the form drag from the drag induced by the vegetative cover, the latter is now calculated by means of the vegetative roughness length.

The principal effect of a slightly modified version of the distributed drag parameterization of Beljaars et al. (2004) in our simulations was a reduced deceleration of the near-surface winds over large parts of Hall and Meta Incognita peninsulas. Consequently, the downslope winds had higher speeds near the surface in the experiments employing the parameterization. For instance, the time series of the surface wind speed at point A show the generally higher speeds simulated in the same experiments (Fig. 13a), which are more realistic. It should be noted that this effect of the distributed drag parameterization is somewhat similar to that expected from simply reducing the effective roughness length to values of the same order of magnitude as the vegetative roughness length values. Therefore, this effect appears to be desirable for the Iqaluit region, based on our study and on previous modelling studies with GEM-LAM at 2.5 km resolution that showed improvement in the surface wind at Iqaluit when the effective roughness length was reduced artificially (Ron Goodson, personal communication, March 2007).

Reduced turbulent mixing in stable conditions was produced in the experiments using the modified Lenderink-Holtslag mixing length compared to those employing a Blackadar-type mixing length (Blackadar, 1962). This resulted in slightly stronger low-level inversions in the same experiments, which are more realistic in the Iqaluit region (not shown). Nonetheless, the impact on the wind speed and direction at Iqaluit is small (Fig. 13). The effect of the increased near-surface resolution was also small in the region because the stable boundary was not shallow enough to require higher resolution. However, the situation is completely different over large areas of Cumberland Peninsula characterized by very strong surface inversions. The need for increased vertical resolution here is obvious, the higher resolution runs showing that the artificial thermal decoupling of the surface from the air above could be drastically reduced or even removed by mixing the air closer to the surface. This aspect is definitely worth further investigation not only in that region but also in other high-latitude regions.

7 Conclusions

The atmospheric conditions over southern Baffin Island during the 7–8 November 2006 wind event, when a surface cyclone tracked over the Labrador Sea, may be representative of atmospheric conditions conducive to strong and sustained channelled winds over Frobisher Bay. We investigated the event by means of simulations performed with a limited-area mesoscale numerical model (GEM-LAM 2.5 km) that were validated with surface and upper-air observations at Iqaluit. The focus was on the low-level winds in the Iqaluit region.

The model simulates wind channelling over Frobisher Bay initiated by a barrier jet. The jet develops as a result of low-level blocking of northeasterly winds by the steep orography of Meta Incognita Peninsula near the head of the bay. Subsequently, wind channelling progresses both along and across the bay, being driven primarily by the large-scale pressure gradient force. Its cross-bay development depends on the interaction of the channelled wind with downslope winds that intensify over the lee slopes of Hall Peninsula. These downslope winds are induced by mountain waves generated when winds associated with the cyclone impinge on the eastern slopes of Hall Peninsula. Their intensification could be explained by the confinement of the mountain waves below a mean-state critical level created by directional wind shear.

The observations at Iqaluit support important simulation findings, such as the directional wind shift at Iqaluit caused by the local low-level wind changing from a downslope wind to an along-bay low-level jet. An interesting result is that the best match to the observations was not obtained at the grid point representing Iqaluit, but at a point located three grid points (approximately 8 km) to the west. This could be partly due to the limited accuracy of the representation of the local topography in our 2.5 km resolution model. A short sensitivity study showed that more realistic surface wind speeds were obtained in the Iqaluit region with the simulations using a distributed drag parametrization.

Our investigation shows that the cyclones tracking over the Labrador Sea close enough to southern Baffin Island can simultaneously generate both the pressure gradients conducive to wind channelling over Frobisher Bay and strong downslope winds over the lee slopes of the mountain ridge on Hall Peninsula. In such a case, the two flows would interact with each other, and this would have a strong effect on near-surface winds at Iqaluit. This possibility should be of interest to aviation because of its potential for generating severe low-level turbulence (Hudson et al., 2001).

This study is by no means a comprehensive modelling investigation of the 7–8 November 2006 wind event. Further work could assess, for instance, the impact of increased horizontal resolution in the Iqaluit region, increased vertical resolution of the first few kilometres above the surface, increased horizontal extent of the model domain, and improved representation of the land surface. As for the initial conditions, their accuracy will probably remain questionable in this data-sparse region, especially near the surface. The quality of the simulations with a limited-area model also depends on the

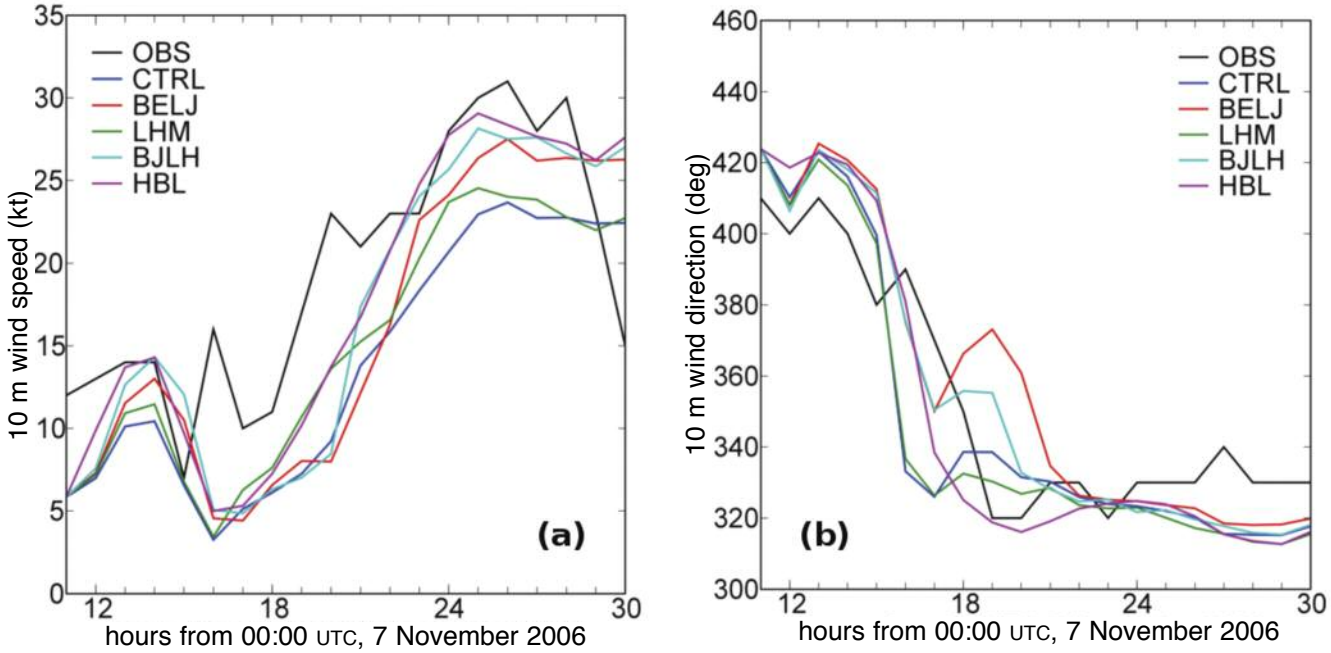

Fig. 13 The observed and simulated time series of surface wind speed (a) and direction (b). The observations were taken at Iqaluit airport, whereas the model data were obtained at point A in the runs considered in the sensitivity study.

accuracy of the lateral boundary conditions. All of these could have an important effect on the simulated downslope and channelled winds and eventually on the winds in the Iqaluit region.

Acknowledgements

We are grateful to Ron Goodson (Environment Canada) for providing us with his report on the effect of the roughness length on the surface wind at Iqaluit in simulations with GEM-LAM 2.5 km, as well as with the geophysical fields used in our runs, satellite images, and Iqaluit wind statistics. We would like to thank Ronald Stewart (University of Manitoba) for the sounding data, which were collected as part of an ArcticNet project. We also thank Jocelyn Mailhot (Environment Canada) for sharing the code of the modified Lenderink-Holtslag mixing length. This work is funded by the Circumpolar Flaw Lead - International Polar Year (CFL-IPY) project and the Storm Studies in the Artic - Canadian Foundation for Climate and Atmospheric Sciences (STAR - CFCAS) network. We would like to thank the two anonymous reviewers for their very constructive comments and suggestions that helped improve our original manuscript. One of the reviewers has suggested a clearer explanation of the cross-bay growth of the channelled wind, which has been included in the paper.

References

BELAIR, S.; J. MAILHOT, C. GIRARD and P. VAILLANCOURT. 2005. Boundary-layer and shallow cumulus clouds in a medium-range forecast of a large-scale weather system. *Mon. Weather Rev.* **133**: 1938–1960.

BELJAARS, A. C. M.; A. R. BROWN and N. WOOD. 2004. A new parametrization of turbulent orographic form drag. *Q. J. R. Meteorol. Soc.* **130**: 1327–1347.

BELL, G. D. and L. F. BOSSART. 1988. Appalachian cold-air damming. *Mon. Weather Rev.* **116**: 137–161.

BLACKADAR, A. K. 1962. The vertical distribution of wind and turbulent exchange in a neutral atmosphere. *J. Geophys. Res.* **67**: 3095–3102.

CARRERA, M. L.; J. GYAKUM and C. LIN. 2009. Observational study of wind channeling within the St. Lawrence river valley. *J. Appl. Meteorol. Climatol.* **48**: 2341–2361.

COLLE, B. A. 2000. High-resolution observations and numerical simulations of easterly gap flow through the Strait of Juan de Fuca on 9–10 December 1995. *Mon. Weather Rev.* **128**: 2398–2422.

COLLE, B. A. and C. F. MASS. 1998a. Windstorms along the western side of theWashington Cascade Mountains. Part I: A high-resolution observational and modeling study of the 12 February 1995 event. *Mon. Weather Rev.* **126**: 28–52.

COLLE, B. A. and C. F. MASS. 1998b. Windstorms along the western side of the Washington Cascade Mountains. Part II: Characteristics of past events and three-dimensional idealized simulations. *Mon. Weather Rev.* **126**: 53–71.

DOYLE, J. D. and Q. JIANG. 2006. Observations and numerical simulations of mountain waves in the presence of directional wind shear. *Q. J. R. Meteorol. Soc.* **132**: 1877–1905.

DURRAN, D. R. 1986. Another look at downslope windstorms. Part I: On the development of supercritical flow in an infinitely deep, continuously stratified fluid. *J. Atmos. Sci.* **43**: 2527–2543.

DURRAN, D. R. 2002. Downslope winds. In: *Encyclopedia of Atmospheric Sciences*. J. Holton, J. Pyle, and J. Curry (Eds), Elsevier Science Ltd., pp. 644–650.

ERFANI, A.; J. MAILHOT, A. METHOT, S. GRAVEL, M. DESGAGNE, A. PLANTE, D. SILLS, P. KING and A. ASHTON. 2006. The 2.5 km horizontal resolution limited area version of the Global Environmental Multiscale model over southern Ontario and Quebec. *In*: Abstracts of 15th International Great Lakes Operational Meteorology Workshop, 25–27 October 2006, Niagara Falls, ON, Canada.

FOUQUART, Y. and B. BONNEL. 1980. Computation of solar heating of the Earth's atmosphere: A new parameterization. *Contrib. Atmos. Phys.* **53**: 35–62.

FUDEYASU, H.; T. KUWAGATA, Y. OHASHI, S. SUZUKI, Y. KIYOHARA and Y. HOZUMI. 2008. Numerical study of the local downslope wind Hirodo-Kaze in Japan. *Mon. Weather Rev.* **136**: 27–40.

GARAND, L. and J. MAILHOT. 1990. The influence of infrared radiation on numerical weather forecasts. *In*: Proceedings of the Seventh Conference on Atmospheric Radiation, 23–27 July 1990, San Francisco, USA.

GOHM, A.; G. J. MAYR, A. FIX and A. GIEZ. 2008. On the onset of bora and the formation of rotors and jumps near a mountain gap. *Q. J. R. Meteorol. Soc.* **134**: 21–46.

GRISOGONO, B. and D. BELUŠIC. 2006. A review of recent advances in understanding the meso- and microscale properties of the severe Bora wind. *Tellus A*, **61**: 1–16.

HANESIAK, J.; R. STEWART, P. TAYLOR, K. MOORE, D. BARBER, G. MCBEAN, W. STRAPP, M. WOLDE, R. GOODSON, E. HUDSON, D. HUDAK, J. SCOTT, G. LIU, J. GILLIGAN, S. BISWAS, D. DESJARDINS, R. DYCK, S. FARGEY, R. FIELD, G. GASCON, M. GORDON, H. GREENE, C. HAY, W. HENSON, K. HOCHHEIM, A. LAPLANTE, R. MARTIN, M. A. MELZER and S. ZHANG. 2010. Storm studies in the Arctic (STAR). *Bull. Am. Meteorol. Soc.* **91**: 47–68.

HUDSON, E.; D. AIHOSHI, T. GAINES, G. SIMARD and J. MULLOCK. 2001. *The Weather of Nunavut and the Arctic*. NAVCanada Report, Ottawa, Ontario, 246 pp.

JIANG, Q. and J. D. DOYLE. 2004. Gravity wave breaking over the central Alps: Role of complex terrain. *J. Atmos. Sci.* **61**: 2249–2266.

KIM, J. and L. MAHRT. 1992. Momentum transport by gravity waves. *J. Atmos. Sci.* **49**: 735–748.

KLEMP, J. B. and D. K. LILLY. 1975. The dynamics of wave induced downslope windstorms. *J. Atmos. Sci.* **32**: 320–339.

KONG, F. and M. K. YAU. 1997. An explicit approach to microphysics in MC2. ATMOSPHERE-OCEAN, **35**: 257–291.

LOESCHER, K. A.; G. S. YOUNG, B. A. COLLE and N. S. WINSTEAD. 2006. Climatology of barrier jets along the Alaskan coast. Part I: Spatial and temporal distributions. *Mon. Weather Rev.* **134**: 437–453.

MAILHOT, J. and A. P. LOCK. 2004. An examination of several parametrizations of mixing lengths in a stable boundary layer: the GABLS case. *In*: Abstracts of The 16th Symposium on Boundary Layers and Turbulence, 9–13 August 2004, Portland, Maine, USA.

MAILHOT, J.; S. BELAIR, L. LEFAIVRE, B. BILODEAU, M. DESGAGNE, C. GIRARD, A. GLAZER, A.-M. LEDUC, A. METHOT, A. PATOINE, A. PLANTE, A. RAHILL, T. ROBINSON, D. TALBOT, A. TREMBLAY, P. VAILLANCOURT, A. ZADRA and A. QADOURRI. 2006. The 15-km version of the Canadian Regional Forecast System. ATMOSPHERE-OCEAN, **44**: 133–149.

MAYR, G. J.; L. ARMI, A. GOHM, G. ZÄNGL, D. R. DURRAN, C. FLAMANT, S. GABERŠEK, S. MOBBS, A. ROSS and M. WEISSMANN. 2007. Gap flows: Results from the Mesoscale Alpine Programme. *Q. J. R. Meteorol. Soc.* **133**: 881–896.

NADEAU, D. 2007. Impacts of synoptic atmospheric circulations and topographic conditions on sustained strong surface winds over southern Nunavut. Master's thesis, McGill University, Montreal, Quebec.

NAWRI, N. 2008. Channelling of high-latitude boundary-layer flow. *Nonlin. Proc. Geophys.* **15**: 33–52.

NAWRI, N. and R. E. STEWART. 2006. Climatological features of orographic low-level jets over Frobisher Bay. ATMOSPHERE-OCEAN, **44**: 397–413.

PARISH, T. R. 1982. Barrier winds along the Sierra Nevada Mountains. *J. Appl. Meteorol.* **21**: 925–930.

SAMELSON, R. M. and P. L. BARBOUR. 2008. Low-level jets, orographic effects, and extreme events in Nares Strait: A model-based mesoscale climatology. *Mon. Weather Rev.* **136**: 4746–4759.

WHITEMAN, C. D. 2000. *Mountain Meteorology: Fundamentals and Applications*. Oxford University Press, New York.

WHITEMAN, C. D. and J. DORAN. 1993. The relationship between overlying synoptic-scale flows and winds within a valley. *J. Appl. Meteorol.* **32**: 1669–1682.

WORTHINGTON, R. M. and L. THOMAS. 1996. Radar measurements of critical-layer absorption in mountain waves. *Q. J. R. Meteorol. Soc.* **122**: 1263–1282.

ZHONG, S.; J. LI, C. D. WHITEMAN, X. BIAN and W. YAO. 2008. Climatology of high wind events in the Owens Valley, California. *Mon. Weather Rev.* **136**: 3536–3552.